

Determining Pavement Design Criteria for Recycled Aggregate Base and Large Stone Subbase

MnDOT Project TPF-5(341)

Task 3 – Construction Monitoring and Reporting

November 2018

Investigators:

Bora Cetin – Principal Investigator
Haluk Sinan Coban – Graduate Research Assistant

Reviewers:

Halil Ceylan – Co-Principal Investigator
Ashley Buss – Co-Principal Investigator
Junxing Zheng – Co-Principal Investigator
William J. Likos – Co-Principal Investigator
Tuncer B. Edil – Co-Principal Investigator

TABLE OF CONTENTS

LIST OF TABLES.....	iv
LIST OF FIGURES	iv
1. INTRODUCTION	1
2. TEST CELLS AND CONSTRUCTION.....	3
2.1. General Overview	3
2.2. Recycled Aggregate Base	5
2.3. Large Stone Subbase.....	5
2.4. Large Stone Subbase with Geosynthetics.....	7
3. PERFORMANCE MONITORING	11
3.1. Environmental Monitoring.....	12
3.2. Dynamic Response Monitoring	13
3.3. Surface Characteristics Monitoring	14
4. DATA COLLECTED DURING AND SHORTLY AFTER CONSTRUCTION	16
4.1. Meteorological Data.....	16
4.2. In-Situ Density and Moisture Content Measurements.....	16
4.3. Dynamic Cone Penetrometer (DCP) Data	20
4.4. Lightweight Deflectometer (LWD) Data	21
4.5. Gas Permeameter Test (GPT) Data	23
4.6. Intelligent Compaction (IC) Data	24
4.7. Falling Weight Deflectometer (FWD) Data.....	28
5. SUMMARY	35
6. REFERENCES	36
APPENDIX A. TEST CELLS ON THE MNROAD LVR AND ROAD LANES	40
APPENDIX B. CROSS-SECTIONS OF TEST CELLS.....	41
APPENDIX C. START AND END STATIONS OF TEST CELLS	43
APPENDIX D. CONSTRUCTION TIMELINE FOR TEST CELLS	44
APPENDIX E. BASE LAYERS OF CELLS 188 AND 189	46
APPENDIX F. BASE LAYERS OF CELLS 127 AND 227	47
APPENDIX G. CONSTRUCTION OF CELLS 128 AND 228	48

APPENDIX H. GEOSYNTHETICS AND CONSTRUCTION OF CELLS 328, 428, 528, AND 628	51
APPENDIX I. LOCATIONS OF THE INSTALLED SENSORS.....	53
APPENDIX J. RELATIVE HUMIDITY, AVERAGE WIND SPEED, AND PRECIPITATION DATA.....	55
APPENDIX K. CBR VALUES ESTIMATED FROM DCP TEST DATA.....	56
APPENDIX L. GPT EQUIPMENT AND TESTED SURFACE TEXTURES	57
APPENDIX M. INTELLIGENT COMPACTION AND ITS CALIBRATION	59
APPENDIX N. RESILIENT MODULI OF RECONSTRUCTED CELLS AT EACH PASS	61
APPENDIX O. FWD TESTING EQUIPMENT	65
APPENDIX P. FWD TEST RESULTS OF CELLS AFTER PAVING.....	66

LIST OF TABLES

Table 2.1. Gradation requirements of base layer materials (MnDOT 2018) (numbers represent total percent passing).....	5
Table 3.1. Type and number of sensors installed (Van Deusen et al. 2018)	11

LIST OF FIGURES

Figure 2.1. (a) Location and (b) traffic lanes of the MnROAD LVR	3
Figure 2.2. (a) Layout and (b) compositions of test cells (not to scale) (s. granular borrow = select granular borrow, TX = triaxial geogrid, GT = geosynthetic, BX = biaxial geogrid).....	4
Figure 2.3. (a) Moisture content adjustment for subgrade soil and (b) prepared subgrade (White and Vennapusa 2017)	6
Figure 2.4. Placement of LSSB material (White and Vennapusa 2017).....	7
Figure 2.5. Pumped subgrade soil in cells 128 and 228 (White and Vennapusa 2017)	7
Figure 2.6. Subbase layers of cells 128 and 227 (Van Deusen et al. 2018)	8
Figure 2.7. (a) Layout and (b) compositions of failed, reconstructed, and remnant cells (not to scale) (TX = triaxial geogrid, GT = geotextile, BX = biaxial geogrid).....	8
Figure 2.8. Placement of (a) geotextile and (b) triaxial geogrid over geotextile (White and Vennapusa 2017)	9
Figure 2.9. Placement of LSSB material over geosynthetics (White and Vennapusa 2017)	10
Figure 3.1. (a) Plan and (b) profile view of sensor locations in cell 186 (s. granular borrow = select granular borrow, TC = thermocouple, EC = moisture probe, PG = dynamic pressure cell, GP = geophone, LE = longitudinal dynamic strain gauge, TE = transverse dynamic strain gauge)	11
Figure 3.2. Thermocouple array in the PVC pipe (MnDOT 2014a).....	12
Figure 3.3. Decagon 5TE moisture probe (MnDOT 2014b)	13
Figure 3.4. Placement of Geokon 3500 dynamic pressure cells (Van Deusen et al. 2018)	14
Figure 3.5. Geophone installed in a borehole (Van Deusen et al. 2018).....	14
Figure 3.6. H-shaped CTL Model ASG 152 dynamic strain gauge (Van Deusen et al. 2018)	14
Figure 3.7. Automated Laser Profile System (APLT) device (Van Deusen et al. 2018).....	15
Figure 3.8. Digital Inspection Vehicle (DIV) (Van Deusen et al. 2018)	15
Figure 4.1. Air temperature data collected from weather stations	16
Figure 4.2. (a) In-situ density and (b) moisture content measurements of cells 185 to 728.....	17
Figure 4.3. Standard Proctor and in-situ density and moisture content values.....	18
Figure 4.4. Density measurements of asphalt layers in cells 185, 127, and 227	18
Figure 4.5. (a) In-situ density and (b) moisture content values of failed, reconstructed, and remnant cells	19
Figure 4.6. Summary of DCPI range of cells 185 to 728	20
Figure 4.7. DCPI values of failed, reconstructed and remnant cells.....	21
Figure 4.8. LWD elastic moduli of cells 185 to 728.....	22
Figure 4.9. LWD elastic moduli of failed, reconstructed, and remnant cells.....	22
Figure 4.10. GPT measurements for cells 185, 186, 188, 189, and 728.....	23

Figure 4.11. Effect of saturation levels on K_{Sat} values.....	24
Figure 4.12. Resilient moduli of cells 127 and 227 at (a) 10 psi (69 kPa) and (b) 30 psi (207 kPa).....	25
Figure 4.13. Composite resilient moduli of cell 328 at each roller pass.....	26
Figure 4.14. Resilient moduli of cells 185 to 728 at (a) 10 psi (69 kPa) and (b) 30 psi (207 kPa).....	27
Figure 4.15. Resilient moduli of failed, reconstructed, and remnant cells at (a) 10 psi (69 kPa) and (b) 30 psi (207 kPa).....	28
Figure 4.16. Water table levels determined by depth-to-bedrock analysis.....	29
Figure 4.17. Maximum deflections of subgrade layers of cells 185 to 189.....	30
Figure 4.18. Composite elastic moduli of subgrade layers of cells 185 to 189.....	30
Figure 4.19. Maximum deflections of cells 185 to 728 before paving.....	31
Figure 4.20. FWD elastic moduli of cells 185 to 728 before paving.....	32
Figure 4.21. Maximum deflections of failed, reconstructed, and remnant cells.....	32
Figure 4.22. FWD elastic moduli of failed, reconstructed, and remnant cells at 5,000 lb (22.2 kN).....	33
Figure 4.23. Maximum deflections of cells 185 to 728 after paving.....	33
Figure 4.24. FWD elastic moduli of cells 185 to 728 at 9,000 lb (40 kN) after paving.....	34
Figure 4.25. Asphalt elastic moduli of cells 185 to 728 at 9,000 lb (40 kN).....	34

1. INTRODUCTION

Approximately 66% of the road network in the U.S. is paved. The majority of traffic loads are carried by the surface course in rigid pavement systems, while such loads are distributed through the sublayers in flexible pavements. More than 90% of the paved roads are flexible pavements with an asphalt surface (Copeland 2011). Since the main working principle of flexible pavements is to distribute loads to the layers beneath the surface course (aggregate base, subbase, and subgrade), the performances of these layers are very important for the long-term pavement performance (Little and Nair 2009; Tutumluer et al. 2015).

The aggregate base course, which is the main load carrying layer, is generally the first layer beneath the asphalt surface course (Cosentino and Kalajian 2001; Yohannes et al. 2009). Base courses are typically constructed using coarse-grained aggregates to provide a stiff and highly permeable layer (Schuettpelez et al. 2010; Haider et al. 2014; Cetin et al. 2014; Edil and Cetin 2015). An adequately stiff aggregate base course reduces overlying pavement deformation and thus increases the lifespan of the pavement (Edil et al. 2012). High stiffness of the aggregate base layer also improves stability of the sublayers by improving the vertical load distribution (Zornberg 2017). Subbase layers are constructed to minimize potential instability of fine-grained subgrade soils due to frost-heave and thaw-weakening and to protect the upper layers (surface and aggregate base courses) as well as to act as a filter between fine-grained subgrade soils and aggregate bases. The porous structure of the subbase layer minimizes capillary action, provides drainage for water infiltrating from the top layers (Uhlmeier et al. 2003; Zornberg 2012), and creates a working platform over weak and soft subgrade soils (Schuettpelez et al. 2010; Kazmee et al. 2016).

About 1.33 billion tons of virgin aggregates (VAs) were produced in the U.S. in 2017 with around 76% used for pavement construction (USGS 2018). The price of VAs has increased due to increasing demand, loss of natural sources, and federal or local restrictions regarding aggregate production (ACPA 2010). These reductions in the availability and cost-effectiveness of VAs have directed researchers' and contractors' attention to alternative materials (Westover et al. 2007). Use of recycled aggregates for base layer construction is a promising approach since recycled aggregate bases (RABs) can perform equally as base layers constructed with VAs and has positive environmental consequences by reducing consumption of natural sources, improving waste utilization, and decreasing greenhouse gas emissions and energy consumption (Lee et al. 2010). In addition, using RAB materials can provide overall project savings by minimizing transportation costs for VAs and decreasing disposal costs when recycled materials are generated and used in place (Gonzalez and Moo-Young 2004), e.g., up to 30% of cost saving could be achieved by the in-place recycling (Edil 2011).

Recycled concrete aggregate (RCA) and recycled asphalt pavement (RAP) materials have been used by several state departments of transportation (DOTs) in hot mix asphalt (HMA) mixtures and in aggregate base layers. RCAs are produced by crushing and processing the existing hardened concrete from old pavement surfaces or from other structures (e.g. buildings and bridges) and removing the construction debris and steel reinforcement (Edil et al. 2012; LRRB 2016). RAP materials are produced by milling old or failed asphalt pavement surfaces to a specific depth (depending on the asphalt course thickness) and processing the milled material (Edil 2011). RCAs are hydrophilic materials due to the presence of concrete mortar residue containing unhydrated

cement (Edil 2011; Edil et al. 2012; Rahatdjo et al. 2010). On the other hand, RAP materials show hydrophobic properties due to the presence of asphalt coating and tend to have a higher saturated hydraulic conductivity than RCAs and VAs (Rahardjo et al. 2010; Nokkaew et al. 2012). RCA and RAP materials have been shown to have higher resilient moduli than VAs (MacGregor et al. 1999; Bennert et al. 2000; Kuo et al. 2002; Cosentino et al. 2003; Abdelrahman et al. 2010; Edil et al. 2012; Stolle et al. 2014; Rosa et al. 2017). RAP materials are less susceptible to water than VAs due to their hydrophobic properties; hence, moisture-induced changes are relatively less important for RAP materials than VAs (Cosentino et al. 2003). Due to hydration of their cement content, RCAs can show an increase in California Bearing Ratio (CBR) values in the soaked condition, which is the condition typically most critical for other aggregates (Jayakody et al. 2012; Garach et al. 2015; Bestgen et al. 2016).

Use of other alternative materials such as unconventional large stones to improve the sustainability of pavement systems is also becoming popular. Using large stones for subbase construction [large stone subbase (LSSB)] or working platforms, for example, has been investigated by the Idaho Transportation Department (ITD), Illinois DOT (IDOT), and Wisconsin DOT (WisDOT) (Uhlmeier et al. 2003; Kazmee et al. 2015; Kazmee et al. 2016). LSSB materials generally go through a single crushing operation; thus, the energy required to break up the stones to obtain conventional size aggregates can be significantly reduced (Kazmee et al. 2015). Although field modulus values of LSSB layers tend to fluctuate when measured by conventional in-situ testing equipment due to the presence of larger voids, LSSB layers can show relatively high stiffness values (Kazmee et al. 2016). Due to the large particle sizes and corresponding limitations of laboratory facilities, however, the engineering characteristics of LSSB materials cannot be easily measured in the laboratory. As a result, limited information is available in the literature regarding the engineering properties of LSSB materials (Schuettelpelz et al. 2010; Kazmee and Tutumluer 2015).

The main objective of this task is to provide a general construction evaluation of test cells built with RAB and LSSB layers. Detailed information is provided regarding the construction of test cells, performance monitoring systems and their applications along test cells. Evaluation of in-situ testing data collected during and shortly after the construction of test cells is summarized. After the detailed literature review, this task is the second stage of a series of subsequent tasks which will include laboratory assessments of the RAB and LSSB materials and in-depth long-term performance analyses of test cells constructed with RAB and LSSB layers.

2. TEST CELLS AND CONSTRUCTION

2.1. General Overview

The field study is being conducted on eleven test cells constructed on the Minnesota Road Research Project (MnROAD) Low Volume Road (LVR), which is a pavement test facility owned by the Minnesota Department of Transportation (MnDOT). The MnROAD LVR, a two-lane closed loop, is located near westbound I-94, northwest of the Twin Cities, MN [Figure 2.1(a)]. Traffic on the MnROAD LVR is simulated by the MnROAD truck, which is a 5-axle tractor/trailer combination weighing 80 kip (36.3 Mg) (MnDOT 2013). The MnROAD truck makes approximately 70 laps per day and it is operated in the inside lane only [Figure 2.1(b)]. The outside lane is dedicated to installing relevant sensors to investigate environmental effects and dynamic responses of select test cells (Van Deusen et al. 2018). Appendix A shows all test cells constructed on the MnROAD LVR and provides more information about the road lanes.

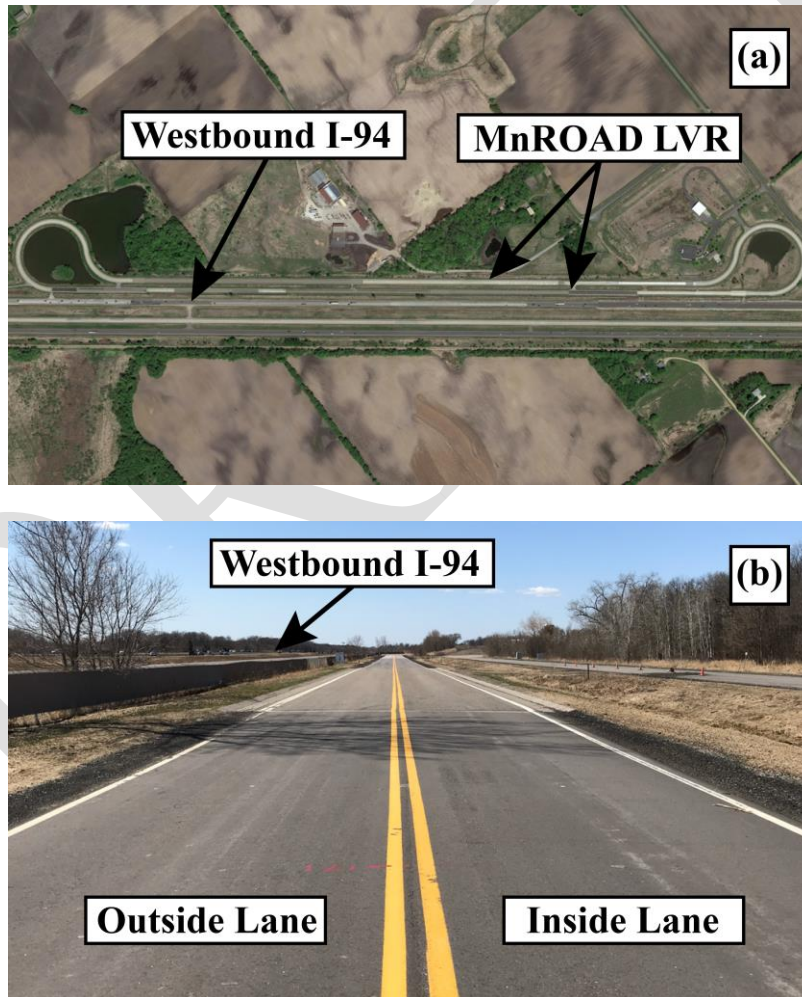


Figure 2.1. (a) Location and (b) traffic lanes of the MnROAD LVR

A layout of test cells and their compositions are provided in Figures 2.2(a) and (b), respectively. Cross-sections and start and end stations of test cells are provided in Appendices B and C,

2.2. Recycled Aggregate Base

Cells 185, 186, 188, and 189 were designed to be approximately 200 ft (61 m) long [width of each lane is about 12 ft (3.7 m)]. Cells 185 and 186 were constructed over a sand subgrade soil. Cells 188 and 189 were constructed on A-6 clay loam subgrade soil (AASHTO M 145). 3.5-in (89-mm) subbase layers overlying the subgrade soils were constructed with similar select granular borrow materials [passing ratio between No. 200 and 1 in (25.4 mm) sieves is less than 12% by mass (MnDOT 2018)]. As stated, coarse RCA, fine RCA, and RCA+RAP blend were used to construct 12-in (305-mm) thick RAB layers in cells 185, 186, and 189, respectively. Limestone aggregate was also used to construct one 12-in (305-mm) thick aggregate base layer (in cell 188) as a control. A comparison between built base layers of cells 188 (limestone base) and 189 (RCA+RAP base) are provided in Appendix E. Each cell was covered with a 3.5-in (89-mm) thick 0.5 in (12.5 mm) NMAS Superpave course in two lifts [first and second lifts were 2.0-in (51-mm) and 1.5-in (38-mm) thick, respectively] (Van Deusen et al. 2018).

Table 2.1. Gradation requirements of base layer materials (MnDOT 2018) (numbers represent total percent passing)

Sieve Size	Coarse RCA (Class 5Q)	Fine RCA (Class 5)	Limestone (Class 6)	RCA+RAP (Class 6)	Aggregate (Class 6)	Aggregate (Class 5Q)
2 in	100	100	-	-	-	100
1 1/2 in	-	-	100	100	100	-
1 in	65-95	-	-	-	-	65-95
3/4 in	45-85	45-100	70-100	70-100	70-100	45-85
3/8 in	35-70	25-90	45-85	45-85	45-85	35-70
No. 4	15-45	15-65	35-70	35-70	35-70	15-45
No. 10	10-30	10-45	20-55	20-55	20-55	10-30
No. 40	0-20	0-20	10-30	10-30	10-30	5-25
No. 200	0-6	0-6	3-7	0-7	3-7	0-10

2.3. Large Stone Subbase

Cells 127 and 227 were designed to be approximately 260 ft (79.2 m) long [width of each lane is about 12 ft (3.7 m)]. Both cells were constructed on A-6 clay loam subgrade soil (AASHTO M 145). A very non-traditional subgrade preparation procedure was followed to create a weak subgrade with a dynamic cone penetration index (DCPI) value between 2.5 and 3.5 in/blow (63.5 and 89 mm/blow) (ASTM D6951) for the upper 1 ft (0.3 m) of the subgrade soil. After constructing the subgrade to the desired elevation, the upper subgrade soil was loosened using shanks mounted to the back of a tracked dozer. Samples from the subgrade soil were taken to check moisture content. It was observed that the moisture content values were far below the optimum moisture content. A water truck was used to supply water to reach the target moisture content [Figure 2.3(a)]. The watered subgrade soil was mixed with dozer/ripper to obtain a somewhat uniform layer for the upper subgrade layer [Figure 2.3(b)]. Repetitive DCP tests (ASTM D6951) were performed to check whether the intended DCPI value was achieved. Minimum and maximum numbers of blows were determined as 3 and 5, respectively, to obtain 12 in (304.8 mm) of penetration in order to be within the target DCPI values. However, the higher end was relaxed as the construction schedule

did not permit a waiting period for drying the soil (David Van Deusen, personal communication). The loosened subgrade soil at the optimum moisture content was mellowed overnight and checked to ensure that the subgrade soil satisfied the strength requirements. Then, LSSB material [3-6+ in (76-152+ mm)] was placed on top of the prepared subgrade (Figure 2.4) (Van Deusen et al. 2018).

The original design was to construct 18-in (457-mm) thick LSSB layers with 1 lift and 2 lifts for cells 127 and 227, respectively. However, cell 227 was also constructed with 1 lift similar to cell 127 because it was observed that dividing LSSB layer construction into 2 lifts was not practical. After the completion of 18-in (457-mm) thick LSSB layers, 6-in (152-mm) thick aggregate base layers were constructed with class 6 aggregate (Appendix F). Lastly, each cell was covered with a 3.5-in (89-mm) thick 0.5 in (12.5 mm) NMA Superpave course in two lifts [first and second lifts were 2.0-in (51-mm) and 1.5-in (38-mm) thick, respectively] (Van Deusen et al. 2018).



Figure 2.3. (a) Moisture content adjustment for subgrade soil and (b) prepared subgrade (White and Vennapusa 2017)



Figure 2.4. Placement of LSSB material (White and Vennapusa 2017)

2.4. Large Stone Subbase with Geosynthetics

Cells 328, 428, 528, and 628 were designed to be approximately 110 ft (33.5 m) long and cell 728 was designed to be around 130 ft (39.6 m) long [width of each lane is about 12 ft (3.7 m)]. In fact, the original design was to build only two cells (cells 128 and 228) with 9-in (229-mm) thick LSSB layers placed over specially prepared A-6 clay loam subgrade soil (AASHTO M 145) (similar preparation procedure described for cells 127 and 227) with no geosynthetics [each cell was around 250 ft (76.2 m) long]. However, after the placement of LSSB layers, pumping of subgrade soil into LSSB layers (Figure 2.5) and base layer rutting were observed in those cells under construction traffic (Appendix G). A comparison between successfully constructed 18-in thick LSSB layer in cell 227 and failed 9-in thick LSSB layer in cell 128 is provided in Figure 2.6. Surface rutting was also observed shortly after paving the base layers with a 3.5-in (89-mm) thick 0.5 in (12.5 mm) NMA Superpave course (White and Vennapusa 2017); thus, cells 128 and 228 were excavated to subgrade layers for reconstruction [Figures 2.7 (a) and (b)]. Cell 228 could not be fully removed because of the presence of near-surface utilities in an area to the east; thus, around 130 ft (39.6 m) of that cell was kept in place and numbered as cell 728 (Van Deusen et al. 2018).

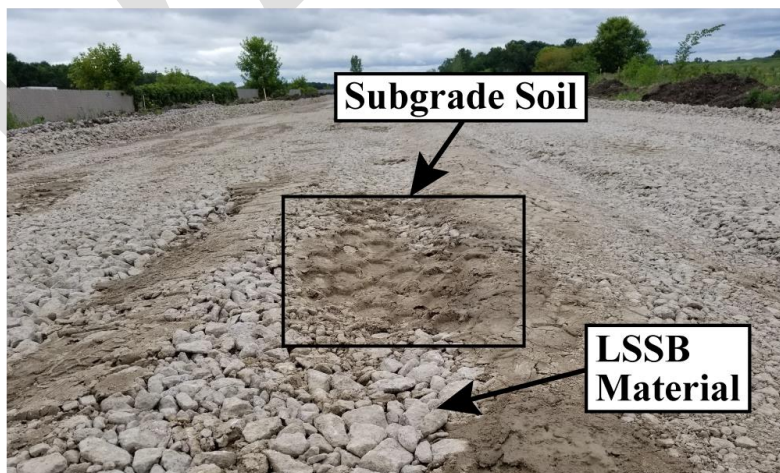


Figure 2.5. Pumped subgrade soil in cells 128 and 228 (White and Vennapusa 2017)

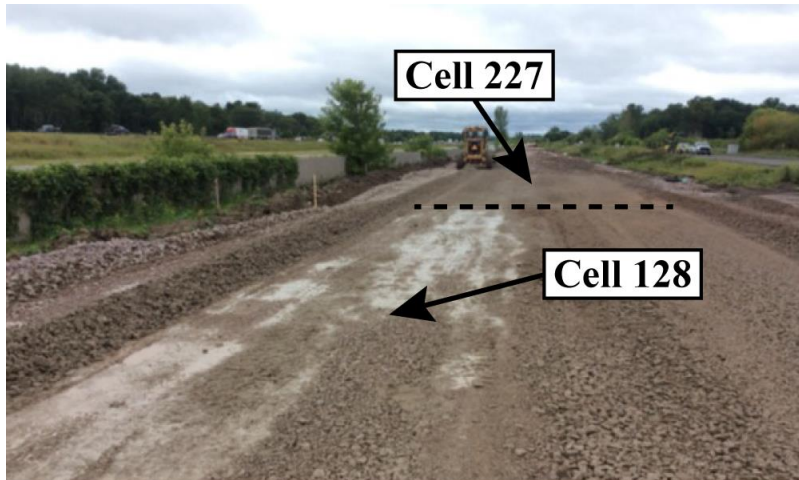


Figure 2.6. Subbase layers of cells 128 and 227 (Van Deusen et al. 2018)

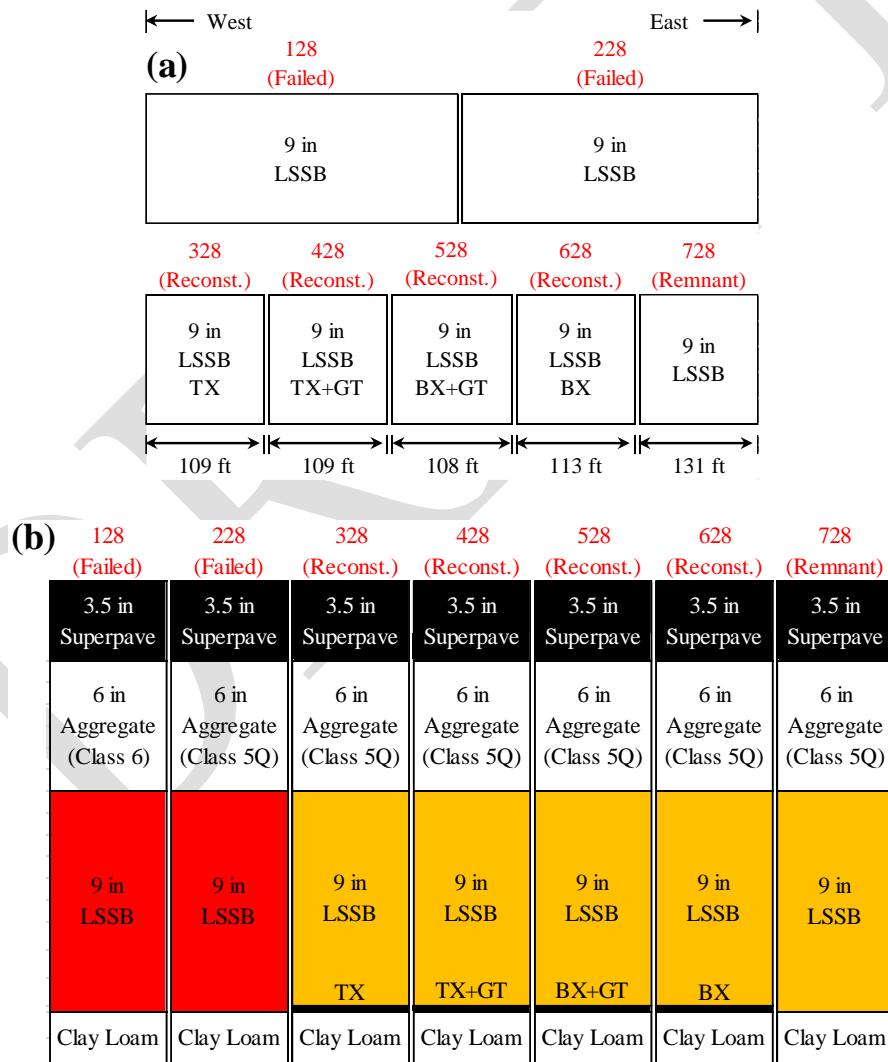


Figure 2.7. (a) Layout and (b) compositions of failed, reconstructed, and remnant cells (not to scale) (TX = triaxial geogrid, GT = geotextile, BX = biaxial geogrid)

Procedures similar to those followed for cells 127 and 227 were used to prepare the subgrade soil for cells 328, 428, 528, and 628. Geosynthetics were placed on top of the subgrade soil to prevent subgrade soil pumping into LSSB layers [Figure 2.8(a)]. More detailed information about geosynthetics used is provided in Appendix H. Tensar TriAx TX190L (triaxial geogrid) was used alone in cell 328 and used with SKAPS GT-116 (needle-punched nonwoven geotextile) in cell 428. In addition, Tensar BX1300 (biaxial geogrid) was used with the same geotextile in cell 528 and used alone in cell 628. Both geogrids were placed over geotextile to obtain the mechanical benefits from interlocking between geogrids and LSSB materials [Figure 2.8(b)]. Coarse-grained aggregates can interlock between grid openings of geogrids and the interlocking mechanism increases the integrity and stiffness of pavement layers (Tutumluer et al. 2010). No geosynthetic was placed in cell 728 since it was not reconstructed. After placing the geosynthetics, 9-inch (229-mm) thick LSSB layers were constructed (Figure 2.9). Class 5Q aggregates were used to construct 6-in (152-mm) thick base layers overlying LSSB layers. After completing the construction of LSSB layers and base layers successfully (Appendix H), all cells except cell 728 were paved with similar asphalt material (cell 728 was already paved with similar asphalt material) (Van Deusen et al. 2018).



Figure 2.8. Placement of (a) geotextile and (b) triaxial geogrid over geotextile (White and Vennapusa 2017)



Figure 2.9. Placement of LSSB material over geosynthetics (White and Vennapusa 2017)

DRAFT

3. PERFORMANCE MONITORING

Environmental and dynamic response monitoring systems were installed for performance monitoring during the life-span of each cell. Environmental monitoring system includes temperature (thermocouples) and moisture sensors (moisture probes). Dynamic response monitoring system consists of dynamic pressure cells, geophones, and dynamic strain gauges (Van Deusen et al. 2018). Environmental and dynamic sensors were installed in cells 185, 186, 188, 189, 127, and 728 at various depths and offsets (Table 3.1 and Appendix I). An example schematic of locations of sensors is provided in Figure 3.1 for cell 186. Several surface monitoring systems are performed to evaluate surface characteristics of each cell over time.

Table 3.1. Type and number of sensors installed (Van Deusen et al. 2018)

Cell Number	Environmental Sensors		Dynamic Response Sensors		
	Thermocouples	Moisture Probes	Dynamic Pressure Cells	Geophones	Dynamic Strain Gauges
185	12	4	2	4	NA
186	12	4	2	4	4
188	12	4	2	4	4
189	12	4	2	4	NA
127	12	3	2	NA	NA
728	16	4	2	NA	4

NOTE: NA = not available.

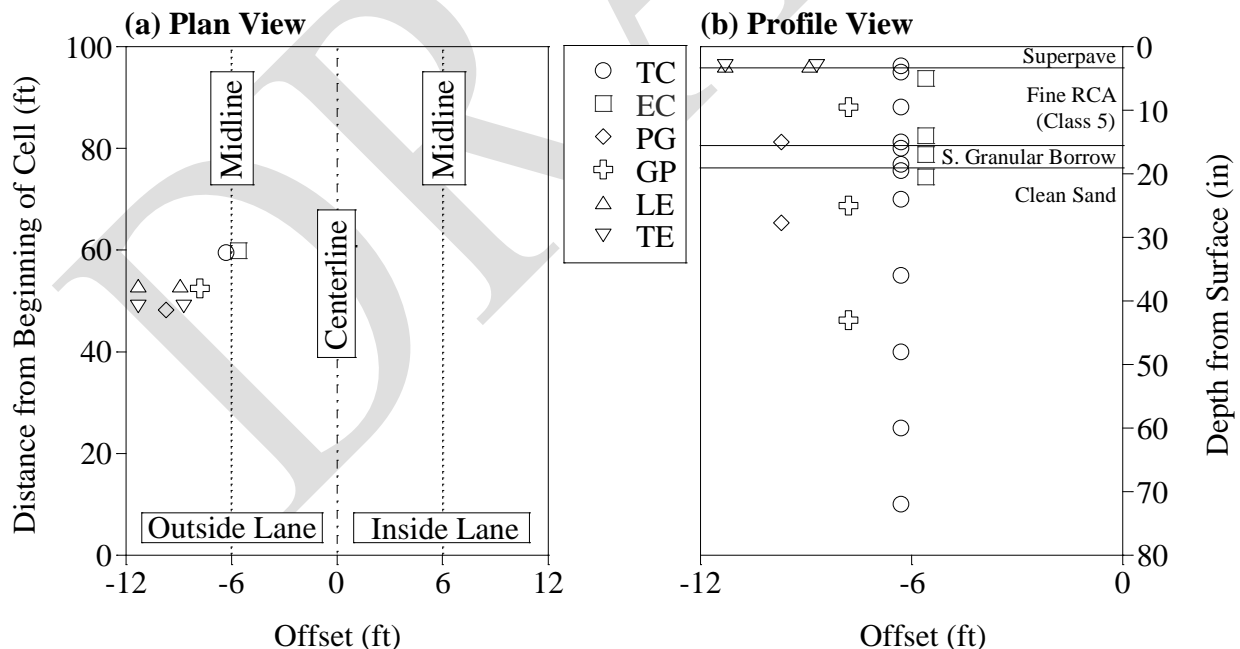


Figure 3.1. (a) Plan and (b) profile view of sensor locations in cell 186 (s. granular borrow = select granular borrow, TC = thermocouple, EC = moisture probe, PG = dynamic pressure cell, GP = geophone, LE = longitudinal dynamic strain gauge, TE = transverse dynamic strain gauge)

3.1. Environmental Monitoring

Thermocouples and moisture probes were installed to determine the annual number of freeze-thaw (F-T) cycles and annual fluctuation of the frost depth of cells in which the sensors were placed. Temperature measurements at various depths are taken by thermocouples which were produced with type T (copper-constantan) thermocouple extension cable at the MnROAD facility. Before the installation of thermocouples, they were attached to a PVC pipe to keep them in place at desired depths (Figure 3.2). Then, the PVC pipe was lowered into a drilled hole (MnDOT 2014a). While 12 thermocouples were installed in cells 185, 186, 188, 189, and 127 at depths ranging from 3 in to 6 ft (76.2 mm to 1.83 m), 16 thermocouples were installed in cell 728 at a similar range of depths (four of them were installed at depths of 0.3, 1, 2, and 3 in below the surface). In addition, while the offsets (from the centerline to the shoulder of the outside lane) of thermocouples are close to the midline of the outside lane in cells 185, 186, 188, and 189 [with offsets ranging from 5.3 to 6.4 ft (1.62 to 1.95 m)], they were installed close to the shoulder of the outside lane in cells 127 and 728 [with offsets around 11.5 ft (3.5 m)]. Temperature readings are taken every 15 minutes (Van Deusen et al. 2018).

Decagon 5TE moisture probes (Figure 3.3), which can measure electrical conductivity, temperature (measured with an internal thermistor), and volumetric water content (calculated based on dielectric permittivity), were installed. The data provided by these gauges will allow characterization of the moisture and soil-water potential regime in pavement structure (MnDOT 2014b). Similar to thermocouples, these gauges were installed at varying depths. While they were installed close to the midline of the outside lane in cells 185, 186, 188, and 189 [with offsets ranging from 4.7 to 5.8 ft (1.43 m to 1.77 m)], they were located close to the shoulder of the outside lane in cells 127 and 728 [offsets were 11 ft (3.35 m)]. In addition, similar to thermocouples, moisture probes were programmed to take readings every 15 minutes (Van Deusen et al. 2018).

In addition to the embedded thermocouples and moisture probes, there are two external weather stations at the MnROAD LVR that record air temperature, atmospheric pressure, relative humidity, precipitation, wind speed and wind direction, and solar radiation. These weather stations are used for the evaluation of representative environmental conditions (Van Deusen et al. 2018).



Figure 3.2. Thermocouple array in the PVC pipe (MnDOT 2014a)



Figure 3.3. Decagon 5TE moisture probe (MnDOT 2014b)

3.2. Dynamic Response Monitoring

Data from dynamic sensors are collected in early spring, late spring, summer, and fall seasons (4 times a year) to evaluate pavement responses over time against vehicle loads. For dynamic response monitoring, the MnROAD truck [5-axle tractor/trailer combination weighing 80 kip (36.3 Mg)] is used at speeds of 5 and 40 mph (8 and 64.4 km/h) for loadings. Tests are conducted at different times of the day to consider the effect of pavement temperature on its performance. FWD tests are performed frequently (throughout spring, summer, and fall months) to evaluate the structural conditions of test cells. In addition, dynamic responses from sensors are also tested and evaluated by FWD testing (Van Deusen et al. 2018).

Geokon 3500 dynamic earth pressure cells were installed with Ashcroft K1 pressure transducers to record vertical pressures present in the base and subgrade layers (Figure 3.4). The pressure transducer records pressure changes from a liquid present between two welded circular plates (6-in diameter plates) of dynamic pressure cell (Van Deusen et al. 2018).

Geophones were only installed in cells 185, 186, 188, and 189 (four geophones per cell). A geophone installed in a borehole at a specific depth can be seen in Figure 3.5. Two geophones were installed approximately 2 ft (0.61 m) below the surface of subgrade both horizontally and vertically. The other two geophones were installed 6 in (152 mm) and 9.5 in (241 mm) below the subgrade and asphalt surfaces, respectively. Displacement values are obtained from geophones which convert the velocity along their axes into a displacement value. They are also used to support the calibration and validation of IC testing (Van Deusen et al. 2018).

H-shaped CTL Model ASG 152 dynamic strain gauges (Figure 3.6) were installed at the bottom of asphalt layers in cells 186, 188, and 728 to record dynamic strains occurring under the asphalt layers due to traffic loads. These sensors were installed in longitudinal and transverse directions by the outer wheel path of the outside lane. Sensors are programmed to collect data four times per year under the load caused by the MnROAD truck [5-axle tractor/trailer combination weighing 80 kip (36.3 Mg)] (Van Deusen et al. 2018).



Figure 3.4. Placement of Geokon 3500 dynamic pressure cells (Van Deusen et al. 2018)



Figure 3.5. Geophone installed in a borehole (Van Deusen et al. 2018)

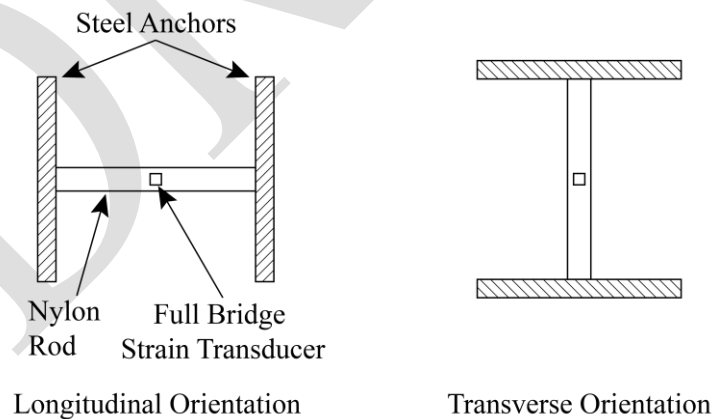


Figure 3.6. H-shaped CTL Model ASG 152 dynamic strain gauge (Van Deusen et al. 2018)

3.3. Surface Characteristics Monitoring

Surface characteristics monitoring is conducted to measure the following parameters: (1) pavement surface distresses (by visual and automated surveys), (2) pavement rutting, and (3) pavement

friction. Visual and automated distress surveys are performed for each cell to record the distress type, extent, and severity. Visual distress surveys are planned to be performed twice a year. Automated distress surveys are planned to be performed more frequently than visual surveys and are compared to the visual distress surveys for verification (Van Deusen et al. 2018).

Automated Laser Profile System (ALPS) (Figure 3.7) and Lightweight Inertial Surface Analyzer (LISA) have been used to measure surface rutting and to obtain profile data, respectively. These data will be compared to the data obtained from Digital Inspection Vehicle (DIV) (Figure 3.8), an advanced surface monitoring vehicle, for verification (Van Deusen et al. 2018). This vehicle is used to evaluate the distress type, extent, and severity along with other surface parameters such as roughness and texture. It can only be operated at temperatures greater than 40°F (4°C) (pavement surface should also be clean) and it is used every two weeks during spring, summer, and fall seasons. After processing the observation data, a summary of the overall pavement condition is obtained (Van Deusen et al. 2018).



Figure 3.7. Automated Laser Profile System (ALPS) device (Van Deusen et al. 2018)



Figure 3.8. Digital Inspection Vehicle (DIV) (Van Deusen et al. 2018)

4. DATA COLLECTED DURING AND SHORTLY AFTER CONSTRUCTION

4.1. Meteorological Data

Meteorological data including air temperature, relative humidity, wind speed, and precipitation were collected by external weather stations located at the MnROAD LVR before, during, and after construction. The variation of air temperature between 7/1/2017 and 12/1/2017 is provided in Figure 4.1. Data regarding relative humidity, average wind speed, and precipitation between the mentioned dates are provided in Appendix J. The minimum and maximum air temperatures were observed to be 40°F (4.4°C) and 91°F (32.8°C) during construction [average temperature was 67°F (19.4°C)]. In addition, relative humidity values ranging between 15 and 102% were observed during construction (Appendix J). Relative humidity values higher than 100% were observed only on 8/10/2017. Except for that day, the maximum relative humidity was 99.7% during construction.

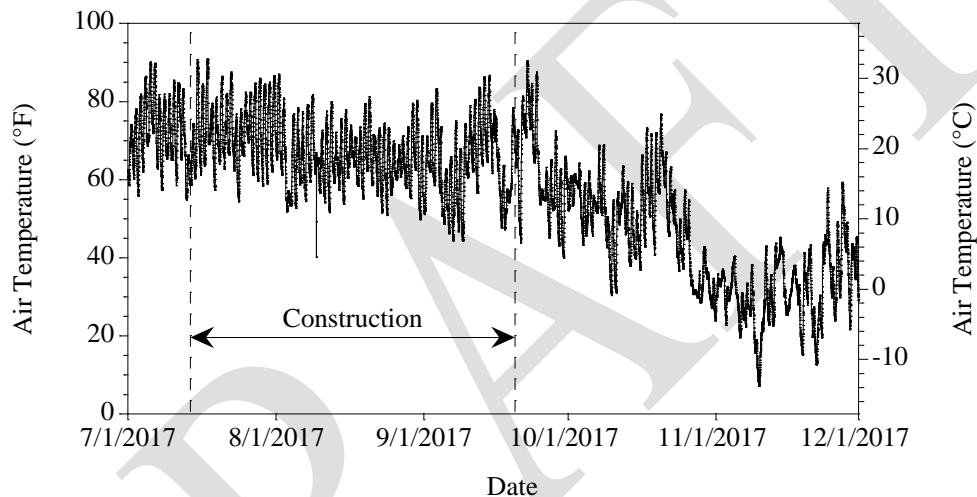


Figure 4.1. Air temperature data collected from weather stations

4.2. In-Situ Density and Moisture Content Measurements

Seaman C-200 NDG was used to measure in-situ density and moisture content data from each cell (MnDOT 2009). Data was collected from subgrade (for cells 185 to 189), base (for each cell), and asphalt (for cells 185, 127, 227) layers. For base and subgrade layers, direct transmission test method was performed at 4, 6, or 8 in depths (depending on the layer thickness) in cases where the test hole stayed open. Backscatter test method was performed when the test hole collapsed due to lack of moisture in the tested layer. For asphalt layers, backscatter test method was used.

Figures 4.2(a) and (b) summarize the in-situ dry density and moisture content data, respectively. Among base layers, limestone base layer in cell 188 provided the highest dry densities and the lowest moisture contents. RCA base layers (in cells 185, 186, and 189) showed lower dry densities and higher moisture contents than limestone base layer in cell 188. In fact, the highest moisture contents were observed with RCA base layers. Class 6 aggregate base layers in cells 127 and 227 provided similar dry densities as RCA base layers; however, they showed lower moisture contents. Class 5Q aggregate base layers in cells 328 to 728 showed the lowest dry density values. Base layer in cell 528 showed the lowest density and moisture content values among these cells. Sandy

subgrades in cells 185 and 186 showed similar dry density and moisture content values. A-6 clay loam subgrades in cells 188 and 189 yielded higher moisture content values than sandy subgrades. Subgrade soil in cell 189 showed the lowest dry density values. Comparisons of dry density and moisture content values obtained from standard Proctor tests and in-situ density and moisture content tests are provided in Figures 4.3(a) and (b), respectively. While in-situ dry density values were higher than the values obtained from standard Proctor testing, in-situ moisture content values were lower than the values obtained from standard Proctor testing.

Figure 4.4 provides in-situ density values of asphalt layers in cells 185, 127, and 227. While the asphalt layer in cell 185 showed a wider density range, similar asphalt in-situ densities [around 141.6 pcf (22.24 kN/m³)] were observed in all cells.

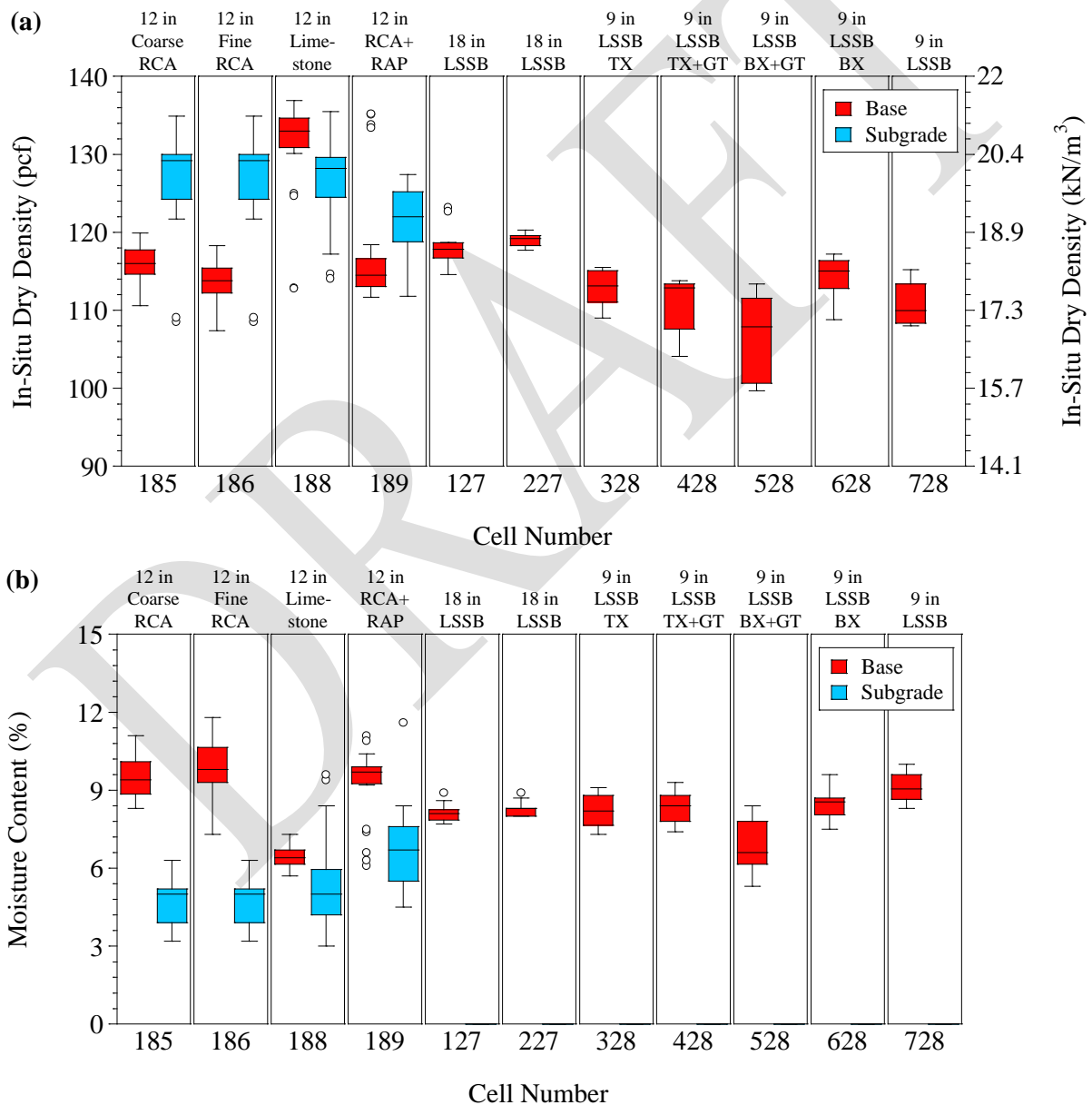


Figure 4.2. (a) In-situ density and (b) moisture content measurements of cells 185 to 728

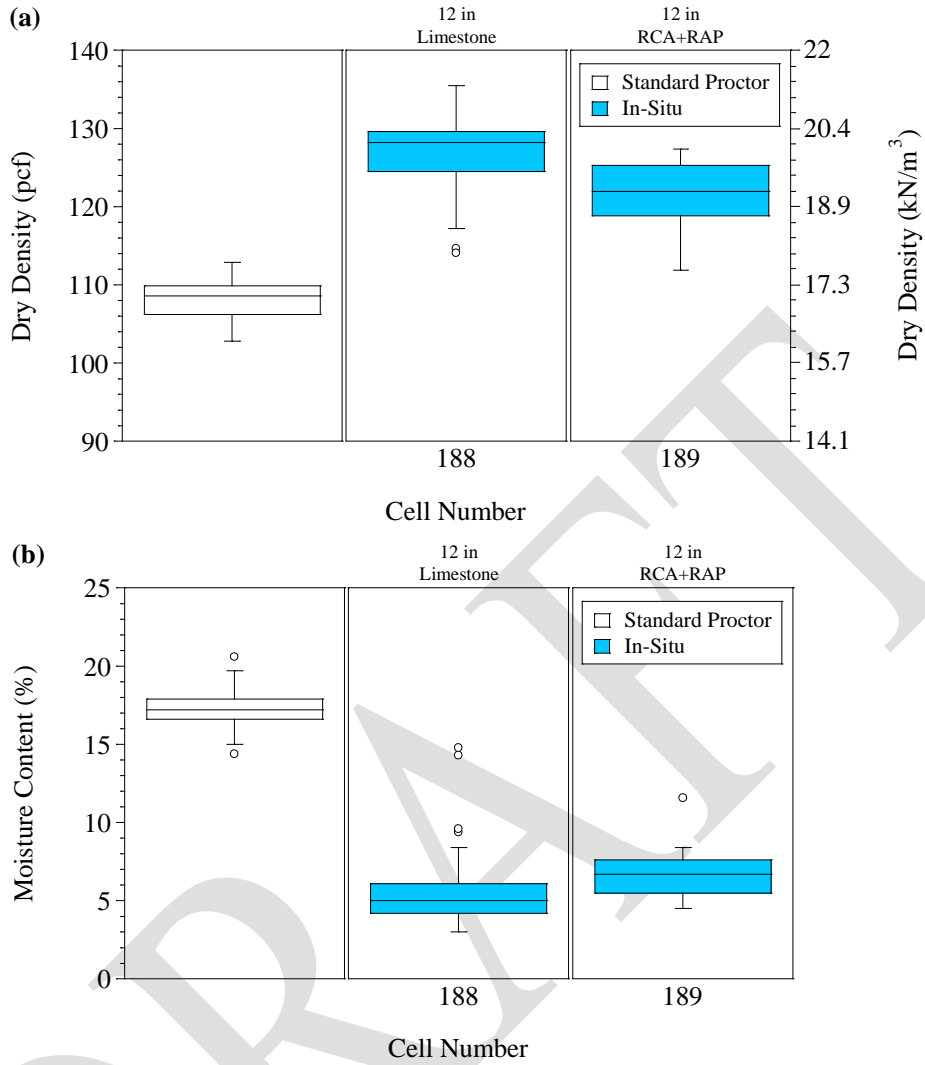


Figure 4.3. Standard Proctor and in-situ density and moisture content values

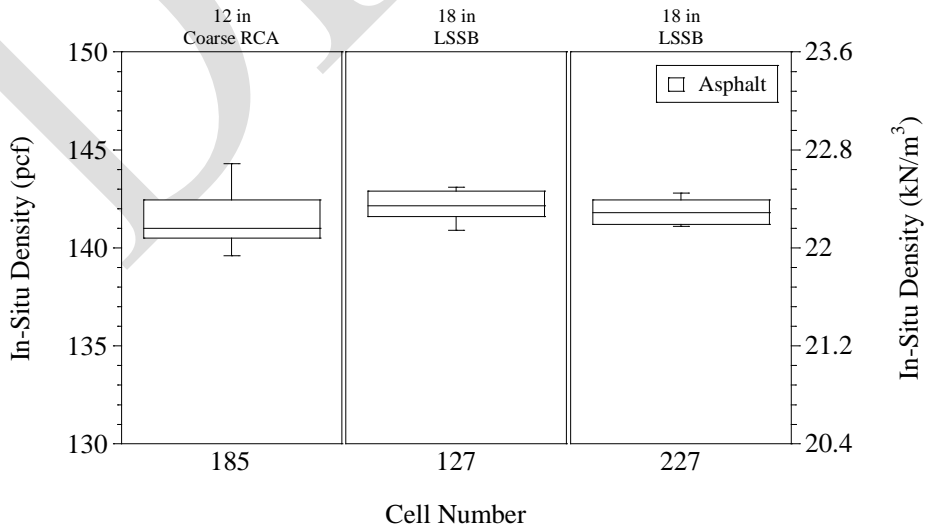


Figure 4.4. Density measurements of asphalt layers in cells 185, 127, and 227

Figures 4.5(a) and (b) show comparisons between failed cells (cells 128 and 228), reconstructed cells (cells 328 to 628) and remnant cell (cell 728) in terms of in-situ dry densities and moisture contents, respectively. Class 6 aggregate base layer of cell 128 showed relatively higher dry densities with no considerable difference in terms of moisture content compared to class 5Q aggregate bases of cells 228 to 728. Again, base layer of cell 528 showed the lowest dry density and moisture content values.

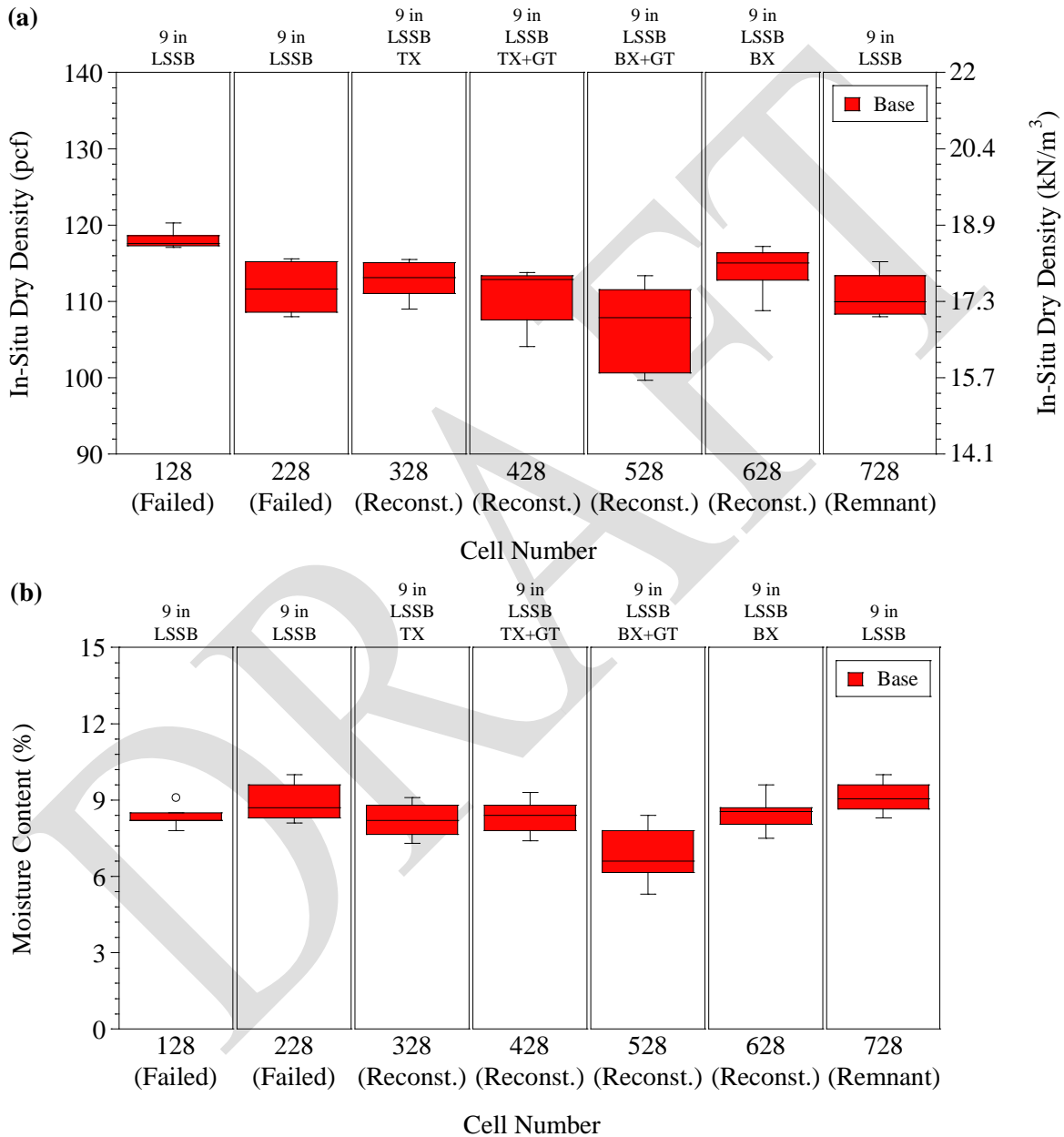


Figure 4.5. (a) In-situ density and (b) moisture content values of failed, reconstructed, and remnant cells

4.3. Dynamic Cone Penetrometer (DCP) Data

DCP tests (ASTM D6951) were conducted on subgrade and base layers of cells during construction. DCP equipment consisted of a 17.6-lb (8-kg) hammer dropped from a height of 22.6 in (575 mm). For base layers of cells 185 to 189, only the depths corresponding to 12 drops were recorded. For base layers of other cells, the target penetration depth was around 6 in (152 mm). Tests could not be performed on subgrade layers of cells 185 and 186 due to rain which resulted in undesired testing condition. For subgrade layers of cells 188 and 189, the drive rod was driven into subgrade layers to a depth of 18 in (457 mm). As stated previously, very soft subgrade conditions were created per project objectives in cells constructed with LSSB layers (cells 127 to 728); thus, traditional DCP testing was not conducted on weak subgrade soils. DCP testing was only used to estimate the target DCPI values [2.5 to 3.5 in/blow (63.5 to 89 mm/blow)] for subgrade soils in these cells. In addition, as stated previously, the higher end was actually kept flexible due to tight construction schedule (David Van Deusen, personal communication).

DCPI values calculated for several points in each cell are summarized in Figure 4.6 and estimated CBR values are shown in Appendix K. Coarse RCA and fine RCA base layers in cells 185 and 186 provided the lowest DCPI values (Figure 4.6). Limestone aggregate base (in cell 188) and RCA+RAP base (in cell 189) also provided relatively lower DCPI values (with no outliers) compared to base layers placed over LSSB layers (in cells 127 to 728). Wider DCPI ranges (mostly with outliers) were observed in base layers constructed over LSSB layers (Figure 4.6).

A comparison between failed cells (cells 128 and 228), reconstructed cells (cells 328 to 628), and remnant cell (cell 728) is provided in Figure 4.7. While relatively narrower DCPI range was observed in the base layer of cell 328, in general, no significant difference was observed between failed cells (cells 128 and 228), reconstructed cells (cells 328 to 628), and remnant cell (cell 728) (Figure 4.7).

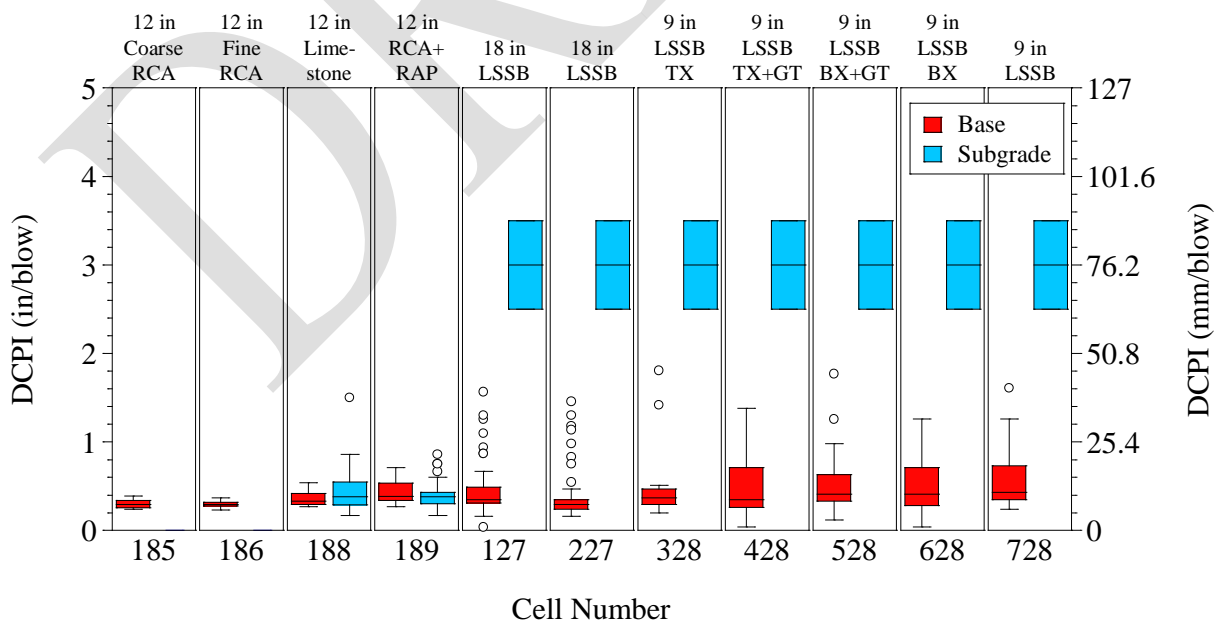


Figure 4.6. Summary of DCPI range of cells 185 to 728

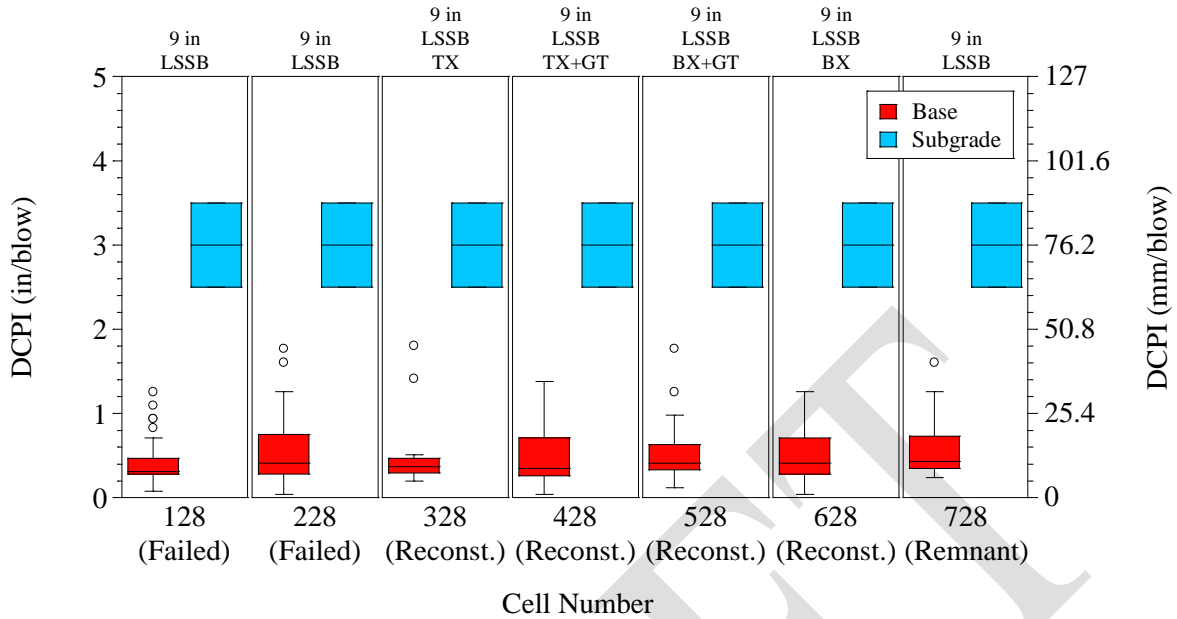


Figure 4.7. DCPI values of failed, reconstructed and remnant cells

4.4. Lightweight Deflectometer (LWD) Data

LWD tests (ASTM E2835) were performed on both subgrade (only for cells 185 to 189) and base layers (for each cell). LWD testing could not be operated on very weak subgrade soils, which were loosened intendedly to construct LSSB layers (for cells 127 to 728). A Zorn ZFG 2000 LWD equipment having a plate diameter of 7.9 in (200 mm), drop mass of 22 lb (10 kg), and drop height of 19.7 in (500 mm) was used for testing [applied load was 1,340 lb (5.96 kN)]. Deflection from the last three drops (out of six drops) were recorded. Deflection values were compared systematically during the last three drops because a difference in deflections of more than 10% would be a sign of an insufficient compaction of the test zone (Siekmeier et al. 2009).

Boussinesq elastic solution was used to derive the LWD elastic modulus (E_{LWD}) of each test point (Vennapusa and White 2009). Parabolic stress distribution was assumed for tests performed on base layers and a shape factor of 8/3 (rigid plate on granular material) was selected to estimate the LWD elastic moduli. On the other hand, inverse parabolic to uniform stress distribution was assumed for tests performed on subgrade layers and the shape factor was selected as $\pi/2$ (rigid plate on material with intermediate characteristics) (Vennapusa and White 2009). In addition, Poisson's ratios of 0.35 and 0.40 were used for tests performed on base and subgrade layers, respectively (Edil et al. 2012).

Figure 4.8 shows LWD elastic moduli (E_{LWD}) calculated from tests performed on base and subgrade layers. Higher elastic modulus values were observed from the tests conducted on base layers of cells 185 to 189 than the tests conducted on subgrade layers of same cells. Tests performed on coarse RCA and fine RCA base layers (in cells 185 and 186, respectively) showed the highest elastic modulus values. Similar median elastic moduli (from tests performed on base layers) were observed in cells 188 to 227 while cells 188 and 189 yielded a relatively wider modulus range. Tests performed on base layers constructed over 9-in (229-mm) thick LSSB layers

(cells 328 to 728) showed the lowest elastic modulus values in general. Particularly, cell 528 showed considerably low elastic modulus values which were as low as 3.43 ksi (23.64 MPa).

A comparison of LWD elastic moduli (E_{LWD} from tests performed on base layers) of failed cells (cells 128 and 228), reconstructed cells (cells 328 to 628), and remnant cell (cell 728) is provided in Figure 4.9. While cells 328, 428, 628, and 728 provided elastic modulus values equal to or greater than the values obtained from cells 128 and 228 which were failed, reconstructed cell 528 had lower elastic modulus than those of failed test cells. No considerable effect of using geosynthetics during reconstruction was observed from LWD data, which is expected since the geosynthetics were placed below LSSB layers.

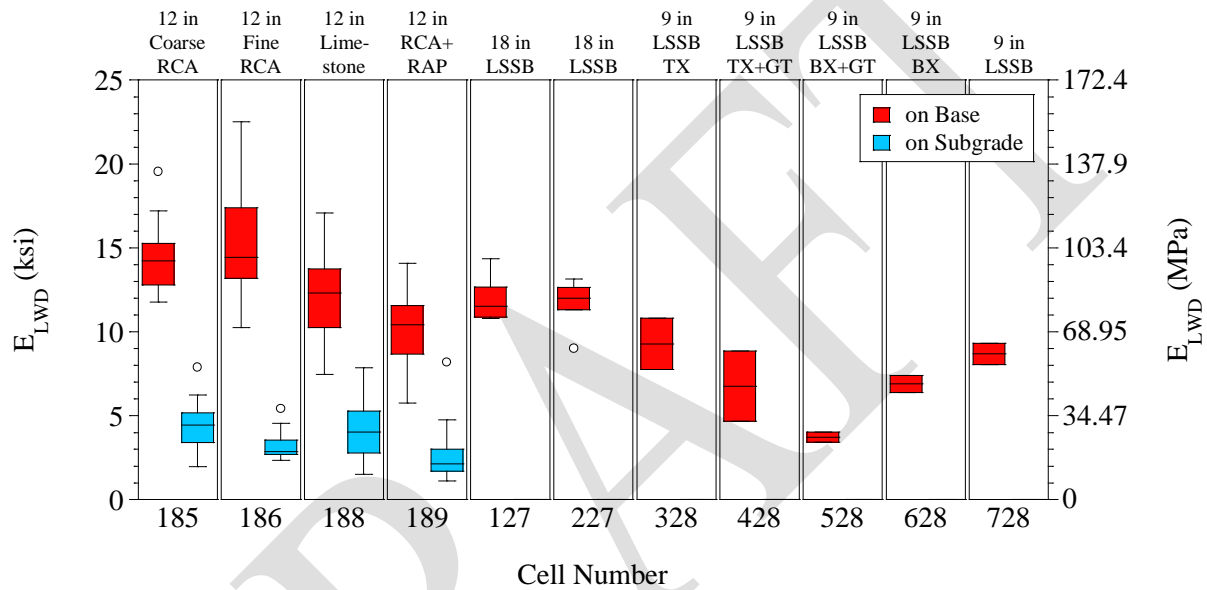


Figure 4.8. LWD elastic moduli of cells 185 to 728

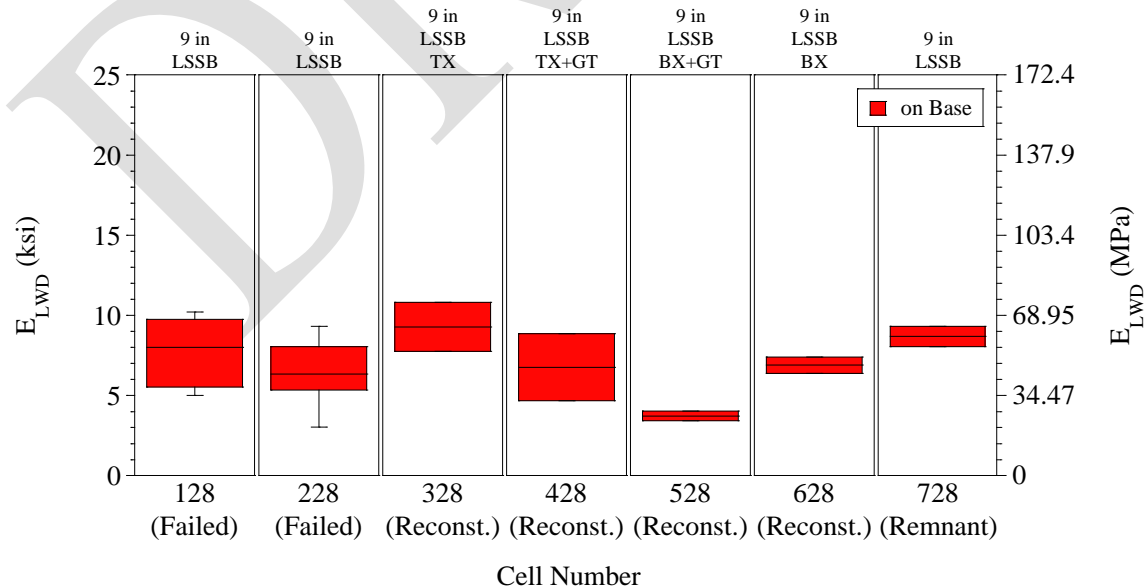


Figure 4.9. LWD elastic moduli of failed, reconstructed, and remnant cells

4.5. Gas Permeameter Test (GPT) Data

A GPT device containing a self-contained pressurized gas system with a self-sealing base plate was used to estimate the saturated hydraulic conductivity (K_{Sat}) of base layers of select test cells (Appendix L) (White et al. 2010). TesCom Model 44-2213-242 regulator and precision orifice were used to control gas flow. Gas flow rate was calculated by digital pressure transducers which were used to monitor the gauge pressure at the inlet and outlet of the orifice. To prevent gas leakage, a polyurethane base seal was attached to the base plate. Saturated hydraulic conductivity (K_{Sat}) values were derived from gas flow and pressure measurements by using Darcy's Law and considering viscosity and compressibility of gas, and gas flow under partially saturated conditions (White et al. 2007). More details are provided in White et al. (2010).

GPT tests were performed only on cells 185, 186, 188, 189, and 728 by following the procedure outlined in White et al. (2010). Two different orifice types were used: (1) GPT(B) with a diameter of 34.29 mils (870.95 mm), and (2) GPT(C) with a diameter of 11.56 mils (293.66 mm) (White et al. 2010). Tests were performed on three different surface textures: (1) fine, (2) medium, and (3) coarse surface textures (Appendix L). Figure 4.10 shows ranges of saturated hydraulic conductivity (K_{Sat}) values based on measurements and in-situ saturation levels. Base layers in cells 186 (fine RCA) and 728 (class 5Q aggregate) provided relatively lower K_{Sat} values. Coarse RCA base layer in cell 185 provided the highest K_{Sat} values.

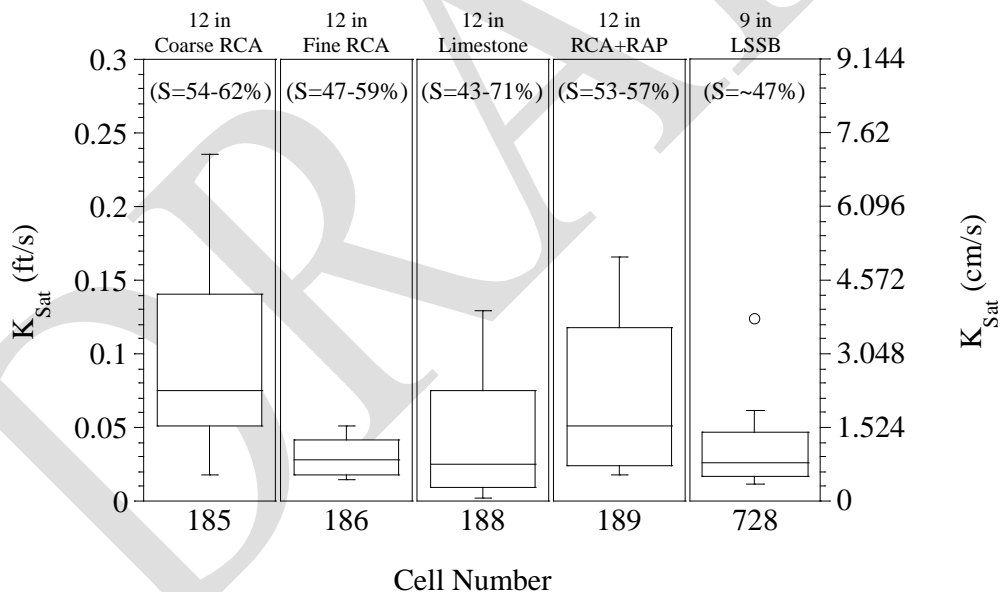


Figure 4.10. GPT measurements for cells 185, 186, 188, 189, and 728 (in-situ saturation levels are shown in parenthesis)

As stated, in Figure 4.10, in-situ density and moisture content values were used to calculate K_{Sat} values. To observe the effect of saturation level (S), three different saturation levels (20, 40, and 60%) were selected and analyses were repeated (Zhao 2011). Figure 4.11 shows the variation of K_{Sat} values with different saturation levels. Lower saturation levels yielded relatively lower K_{Sat} values. In addition, change of K_{Sat} values between $S=40\%$ and $S=60\%$ were relatively higher than changes observed between $S=20\%$ and $S=40\%$.

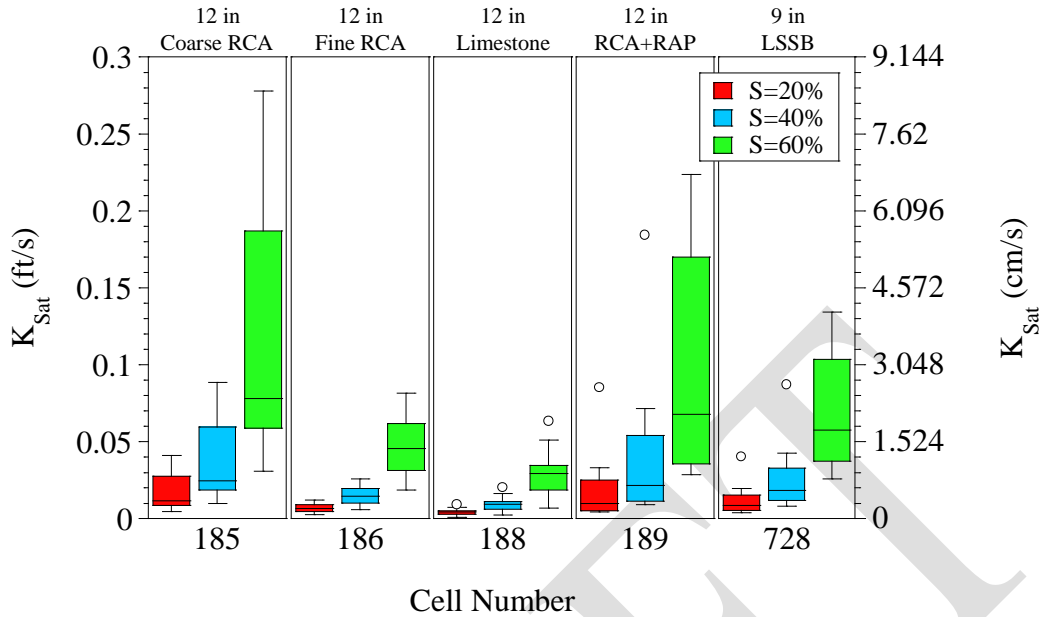


Figure 4.11. Effect of saturation levels on K_{Sat} values

4.6. Intelligent Compaction (IC) Data

The IC field testing, calibrated with automated plate load testing (APLT) to obtain cyclic stress-dependent composite and layered resilient modulus (M_R) values, was performed on subbase layers (only for cells 127 and 227) and base layers (for each cell) of test cells by Ingios Geotechnics. First, preliminary IC mapping results were obtained. Then, several test locations were selected for APLT testing based on the initial IC mapping results. APLT equipment (Appendix M) was used to measure in-situ resilient modulus values directly (White and Vennapusa 2017). For IC testing and mapping, a Caterpillar CS56 vibratory smooth drum roller which weighs about 27,450 lb (122.1 kN) was outfitted with Ingios validated IC retrofit system (Appendix M). Stress-dependent resilient modulus (M_R) values at 10 psi (69 kPa) and 30 psi (207 kPa) plate contact stresses were calculated (White and Vennapusa 2017). More information about IC calibration and data analysis is provided by White and Vennapusa (2017).

For the evaluation of subbase layers, IC testing was only performed on 18-in thick LSSB layers in cells 127 and 227 and their results are shown in Figures 4.12(a) and (b) for both plate contact stresses. While cell 127 showed relatively higher composite and subbase resilient moduli at both stress levels, both cells showed similar subgrade resilient moduli.

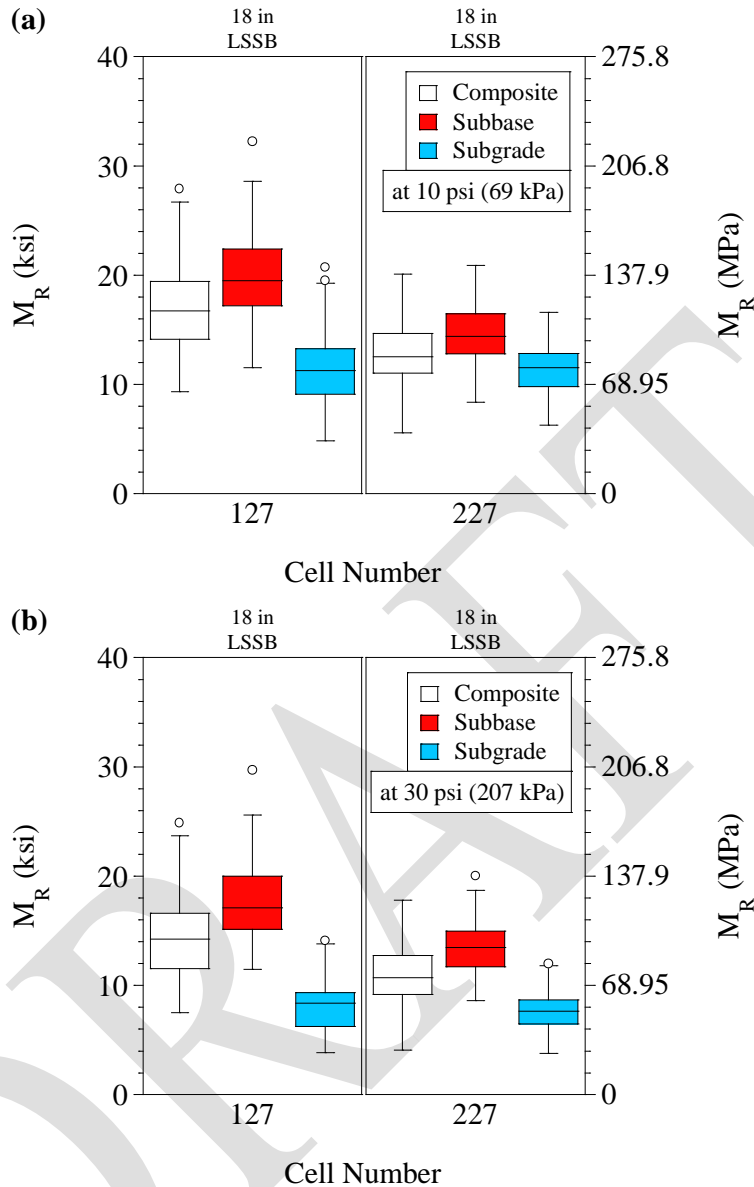


Figure 4.12. Resilient moduli of cells 127 and 227 at (a) 10 psi (69 kPa) and (b) 30 psi (207 kPa)

As stated previously, rutting of subbase and base layers in cells 128 and 228 was observed during construction and in-situ testing (Appendix G). After reconstruction, seven passes were made during mapping of cells 328 to 628. An increase in the number of passes yielded an increase in resilient moduli in these cells and modulus values obtained during the seventh pass (last pass) were used for overall comparison analyses. As an example, composite resilient modulus values of cell 328 during each roller pass is provided in Figure 4.13. Composite, base+subbase (they were combined and assumed as one layer), and subgrade resilient moduli of cells 328 to 628 at each roller pass are provided in Appendix N.

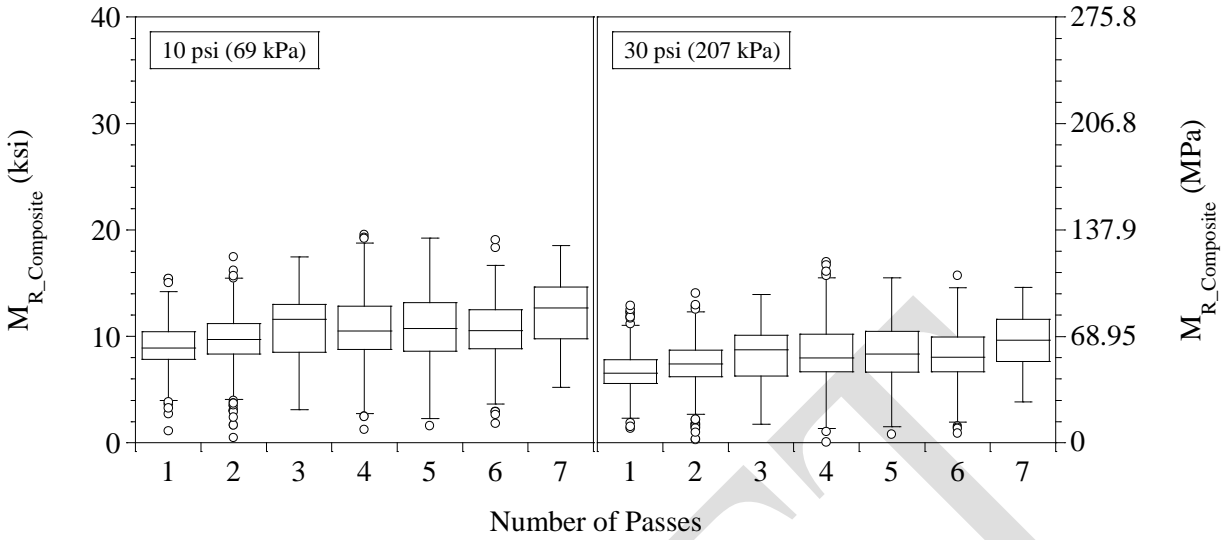


Figure 4.13. Composite resilient moduli of cell 328 at each roller pass

For cells 185 to 728, estimated composite, base+subbase (they were combined and assumed as one layer), and subgrade resilient modulus values at 10 psi (69 kPa) and 30 psi (207 kPa) plate contact stresses levels are summarized in Figures 4.14(a) and (b), respectively. The highest resilient moduli at both stress levels were observed in cells 185 (coarse RCA base) and 186 (fine RCA base). While cell 127 with 18-in (457-mm) thick LSSB layer provided higher resilient moduli than cells 188 (limestone base) and 189 (RCA+RAP base), cell 227 in which the same subbase layer was constructed provided lower resilient moduli. At both stress levels, test cells constructed with 9-in (229-mm) thick LSSB layers (cells 328 to 728) showed the lowest resilient modulus values.

Figures 4.15(a) and (b) provide a comparison of resilient moduli between failed cells (cells 128 and 228), reconstructed cells (cells 328 to 628), and remnant cell (cell 728) at 10 psi (69 kPa) and 30 psi (207 kPa) plate contact stresses levels, respectively. It was observed that reconstructed cell 528 provided the lowest resilient moduli at both stress levels. In addition, it was concluded that cell 728, the remnant of cell 228, had higher resilient moduli than the overall (removed part + remnant part) resilient moduli of cell 228.

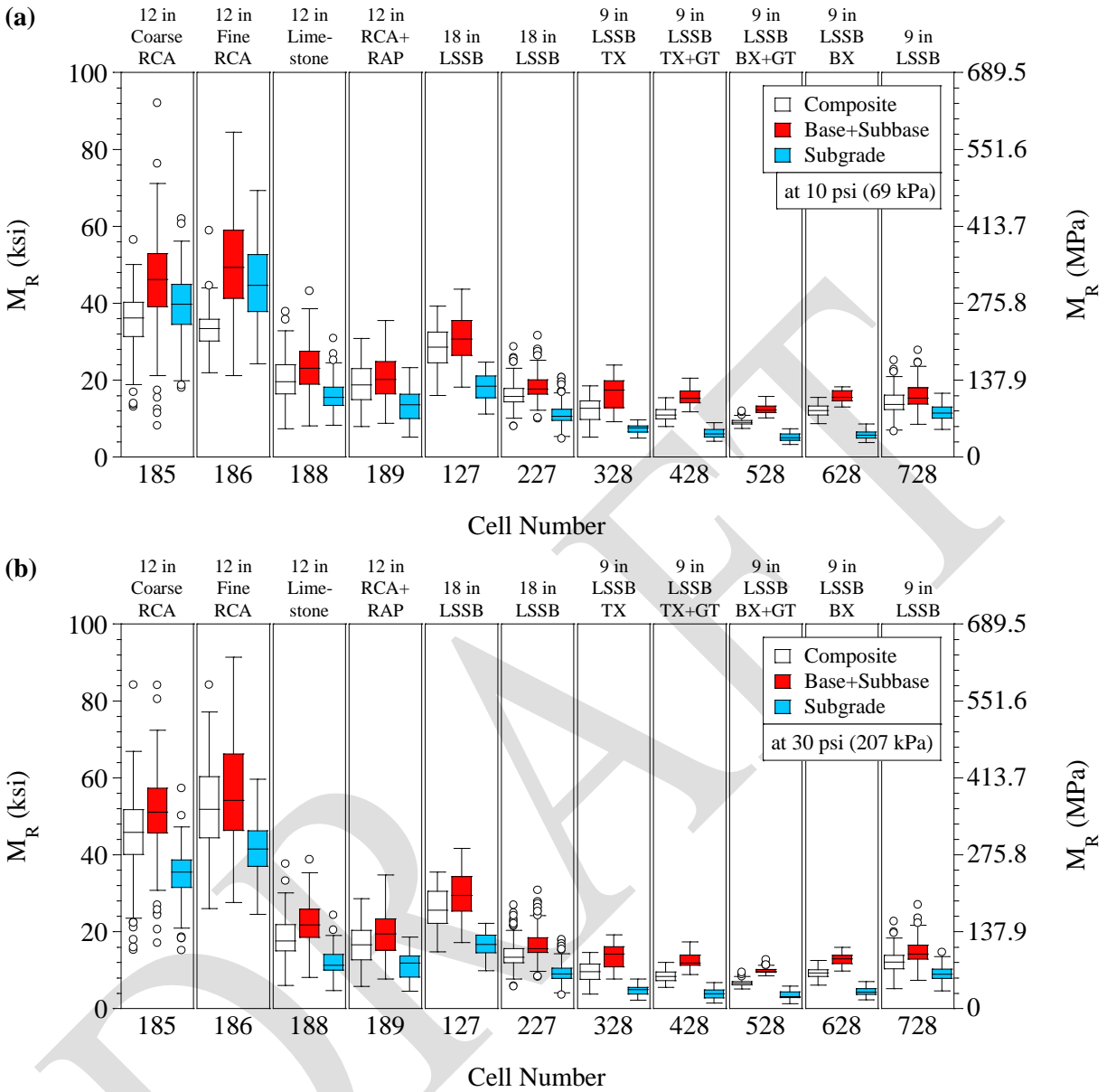


Figure 4.14. Resilient moduli of cells 185 to 728 at (a) 10 psi (69 kPa) and (b) 30 psi (207 kPa)

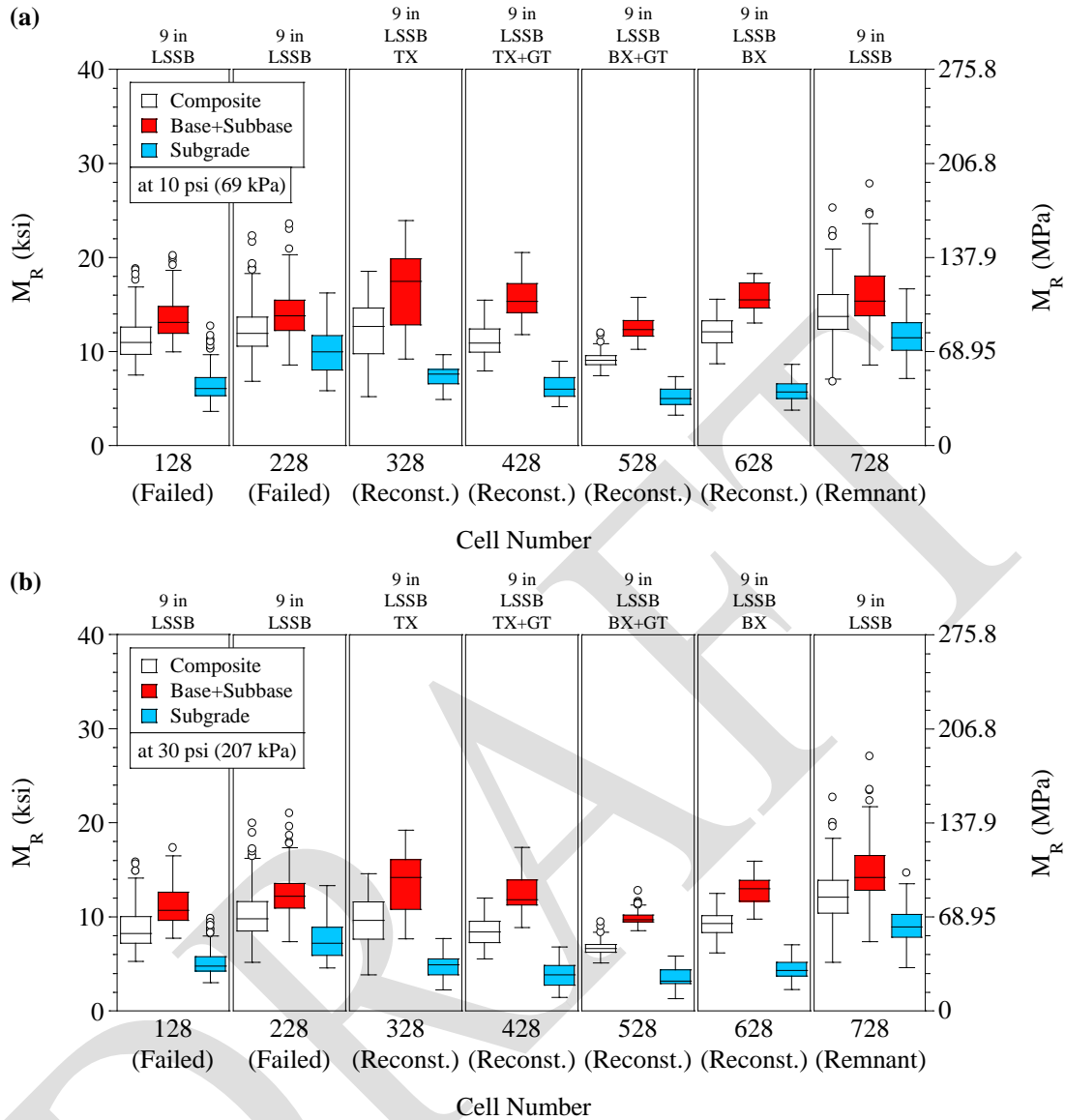


Figure 4.15. Resilient moduli of failed, reconstructed, and remnant cells at (a) 10 psi (69 kPa) and (b) 30 psi (207 kPa)

4.7. Falling Weight Deflectometer (FWD) Data

FWD testing, a non-destructive in-situ testing, was performed during construction and around two months after the final placement of asphalt surfacing to evaluate the deflection and elastic modulus (E_{FWD}) of test cells. A trailer-mounted Dynatest Model 8002 FWD device (Appendix O) with two plate (rigid) diameters [17.7 in (450 mm) for subgrade and base layers, and 11.8 in (300 mm) for asphalt layers] were used. For deflection basin evaluation, eight geophones were located 8 in (203.2 mm), 12 in (304.8 mm), 18 in (457.2 mm), 24 in (609.6 mm), 36 in (914.4 mm), 48 in (1219.2 mm), 60 in (1524 mm), and 72 in (1828.8 mm) away from the center plate where the loading was applied. Three loading drops with increasing load levels were applied. Composite elastic modulus values were calculated by Boussinesq elastic solution (Vennapusa and White 2009) for the maximum deflections measured at the center of the loading plate. The shape factor

was selected as 8/3 (rigid plate on granular material with parabolic stress distribution) for analyses of tests performed on aggregate base layers. For subgrade layers, the shape factor of $\pi/2$ (rigid plate on material with intermediate characteristics with inverse parabolic to uniform stress distribution) was used. Poisson's ratios of 0.30, 0.35 and 0.40 were used for asphalt, base+subbase (they were combined and assumed as one layer) and subgrade layers, respectively (Edil et al. 2012).

Layered elastic modulus analyses were performed by MODULUS 7.0 program which was developed at Texas Transportation Institute (TTI) mainly for flexible pavements. MODULUS 7.0 uses database method for back-calculation and assumes linear-elastic theory to back-calculate elastic moduli from recorded deflection basins during testing (Edil et al. 2012). It uses WESLEA program to create a deflection basin database which is then used to determine the layered modulus values that give deflection basins similar to the actually measured ones (William 1999; Baladi et al. 2011). The program only allows for seven sensors. Thicknesses of asphalt, base, and subbase layers are entered manually, and the program has three options for the subgrade thickness: (1) semi-infinite thickness, (2) depth-to-bedrock analysis, and (3) manual entry (William 1999). In this project, depth-to-bedrock analysis (Rohde et al. 1992; Newcomb et al. 1995) was selected as a result of potential relatively shallow water table. By using the depth-to-bedrock analysis, not only the presence of bedrock but also elevations of stiff clay layer and water table can be estimated (Liu and Scullion 2001; Chatti et al. 2017). Incorrect back-calculation for the upper layers can be made by selecting a semi-infinite subgrade layer when there is a relatively stiff layer (Newcomb et al. 1995). In general, if the stiff layer is deeper than around 450 in (11.43 m), it does not cause a significant effect (Chatti et al. 2017). In MODULUS 7.0, maximum 300 in (7.62 m) can be entered as the subgrade thickness (Liu and Scullion 2001). Figure 4.16 shows water table levels determined for test cells by the depth-to-bedrock analysis. Median values were used for backcalculation. Water table levels in cells 185 and 186 were relatively deeper than water tables in other cells. In addition, subgrade/bedrock modular ratio of 100 is recommended for depth-to-bedrock model. However, a ratio of 5 was used for backcalculation because it was assumed that the stiffening was due to stiff clay soil (saturated soil where water table is high) (Liu and Scullion 2001).

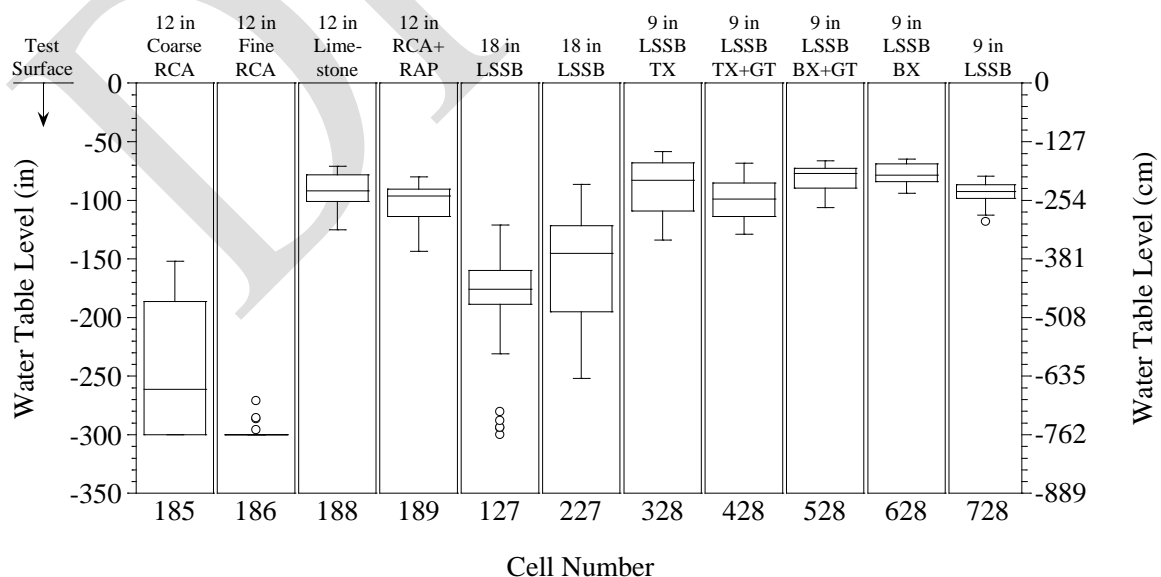


Figure 4.16. Water table levels determined by depth-to-bedrock analysis

During construction, tests were performed on subgrade (only for cells 185 to 189) and base (for each cell) layers. For subgrade layers of cells 185 to 189, at each testing location, three loading drops that ranged between 3,700 lb (16.46 kN) and 7,700 lb (34.25 kN) were applied with increasing load levels and maximum deflections were recorded at the center of the loading plate (Figure 4.17). To calculate elastic modulus values corresponding to deflections, the measured maximum deflections were normalized to 5,000 lb (22.2 kN) and 7,000 lb (31.1 kN) loads, respectively, because seating was observed after the first drop (Figure 4.17). Boussinesq elastic solution (Vennapusa and White 2009) was used to calculate composite elastic moduli of subgrade layers (Figure 4.18). Sandy subgrade layers of cells 185 and 186 provided lower maximum deflections and higher elastic moduli compared to clayey subgrade soils of cells 188 and 189.

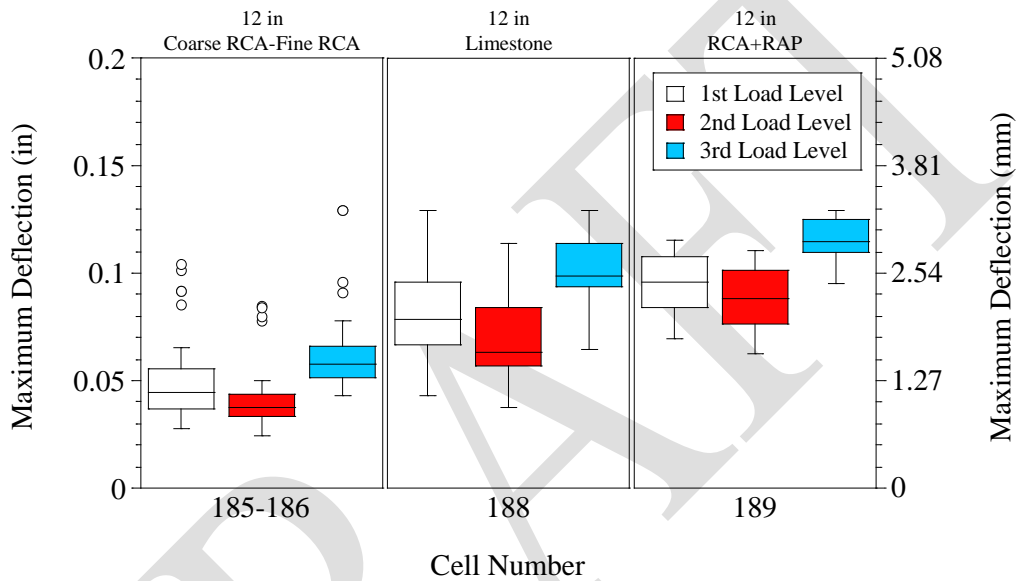


Figure 4.17. Maximum deflections of subgrade layers of cells 185 to 189

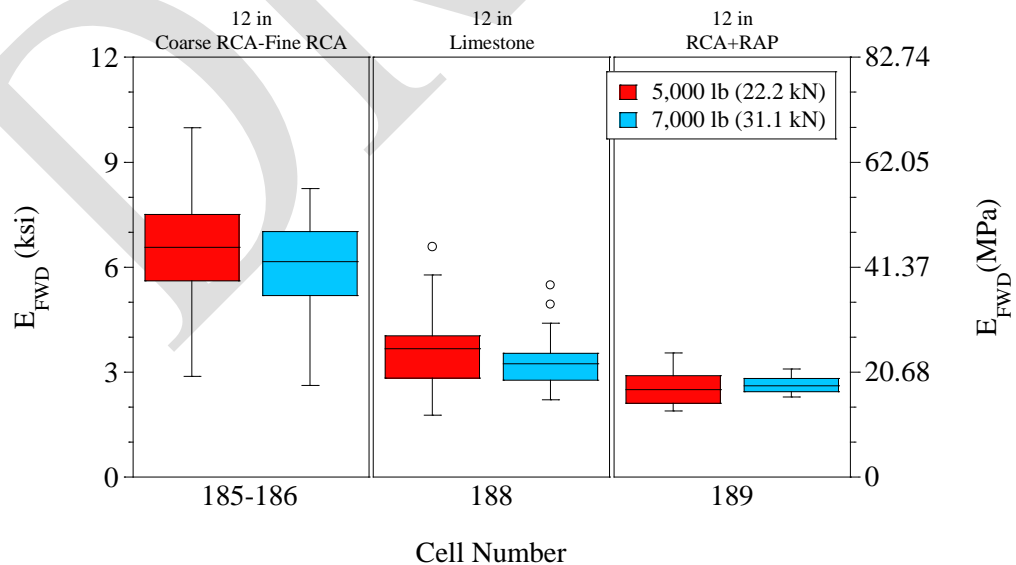


Figure 4.18. Composite elastic moduli of subgrade layers of cells 185 to 189

For base layers of test cells before paving, three loading drops ranged between 1,660 lb (7.38 kN) and 6,080 lb (27.04 kN) were applied with increasing load levels. Maximum deflections measured at the center of the loading plate for cells 185 to 728 are summarized in Figure 4.19. While the first loading drop had the lowest load level, relatively higher maximum deflections were observed compared to the deflections caused by the second loading drop. Therefore, the first loading drop was assumed as a seating drop. As seen in Figure 4.19, the lowest maximum deflections were observed in cells 185 and 186 constructed with coarse RCA and fine RCA base layers, respectively. Cells 188 (limestone base), and 127 and 227 were also provided relatively lower maximum deflections. Cells 328 to 628 yielded relatively higher maximum deflections than other cells (specifically, cell 528 showed the highest maximum deflections). Compared to them, cell 728 provided relatively lower maximum deflections.

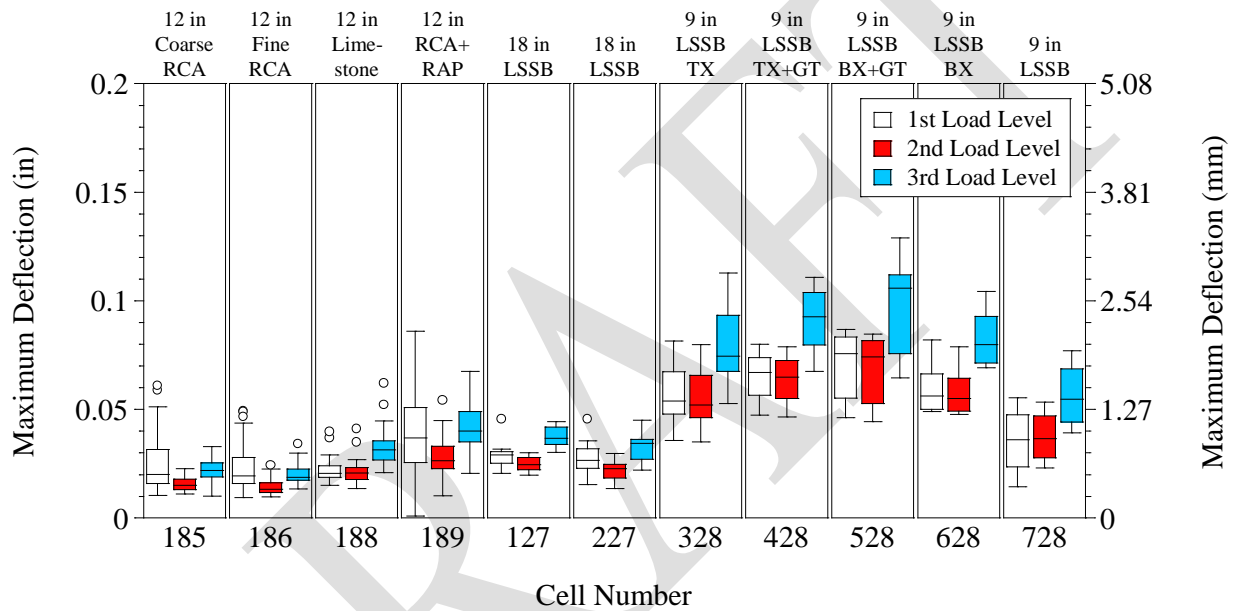


Figure 4.19. Maximum deflections of cells 185 to 728 before paving

Actually, in addition to the first loading drop, the second loading drop was also assumed as the seating drop and composite analysis and back-calculation were performed only for the third loading drop in which the deflections were normalized to a 5,000-lb (22.2-kN) load (Figure 4.20). Since cells 185 and 186 provided the lowest maximum deflections in Figure 4.19, they also provided the highest elastic moduli (Figure 4.20). In addition, the lowest elastic modulus values were obtained for cells 328 to 628, and cell 728 yielded higher moduli than them.

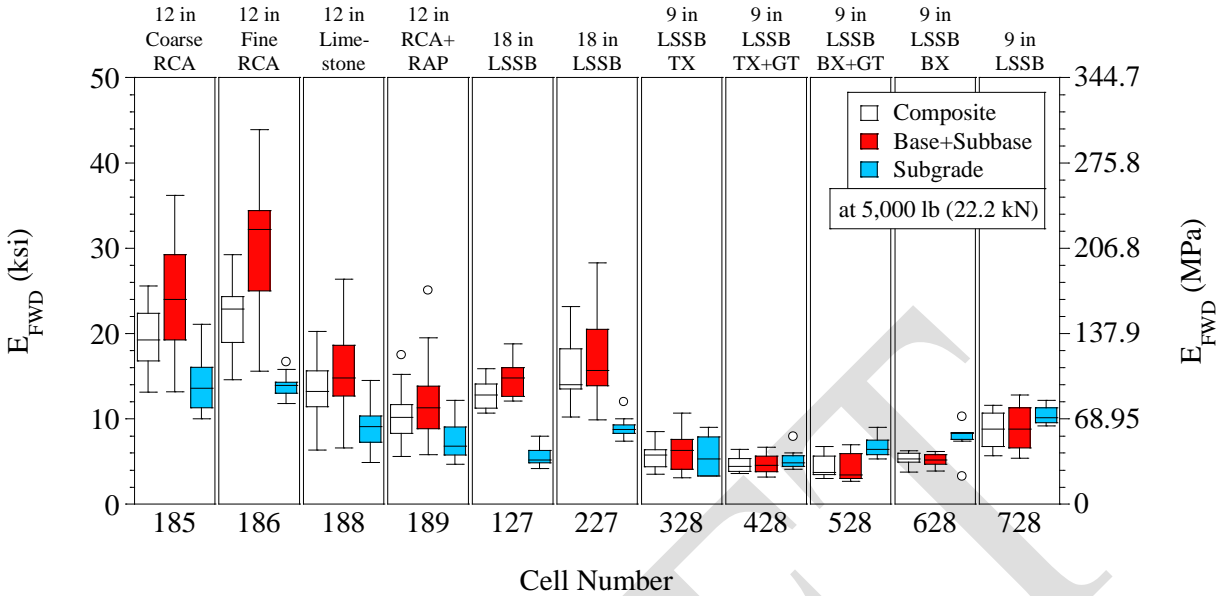


Figure 4.20. FWD elastic moduli of cells 185 to 728 before paving

Comparisons of maximum deflections and elastic modulus values of failed cells (cells 128 and 228), reconstructed cells (cells 328 to 628), and remnant cell (cell 728) are provided in Figures 4.21 and 4.22, respectively. Overall, failed cells (cells 128 and 228) provided relatively lower maximum deflections and higher elastic moduli than reconstructed cells. Since relatively lower maximum deflections and higher elastic moduli were observed in cell 728 (remnant from cell 228) compared to cell 228, it was concluded that cell 728 was the stiffer part of cell 228.

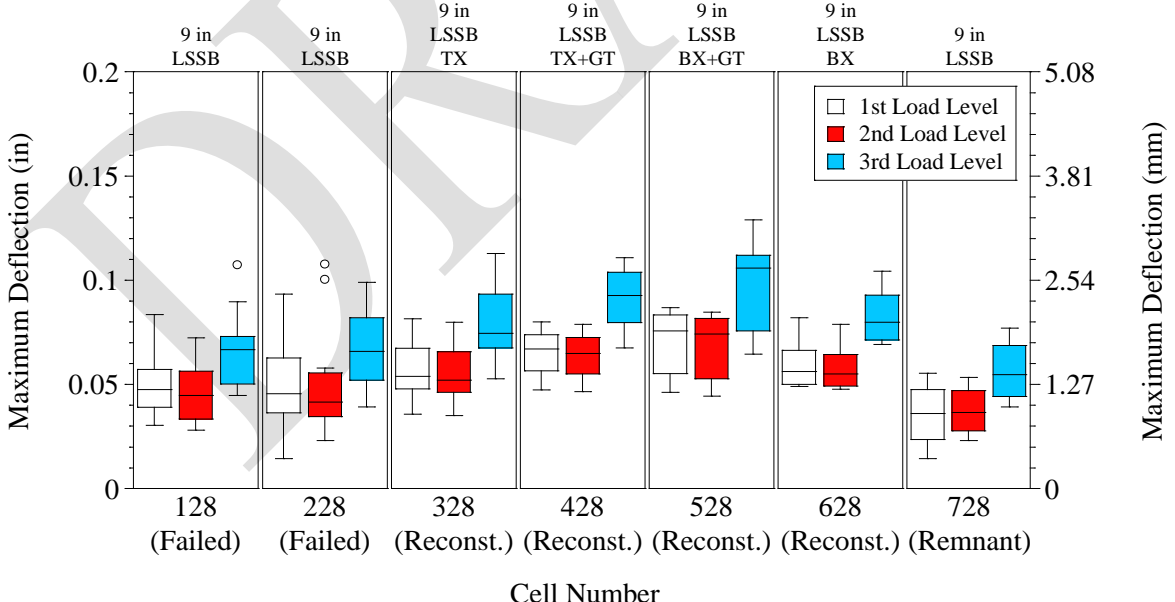


Figure 4.21. Maximum deflections of failed, reconstructed, and remnant cells

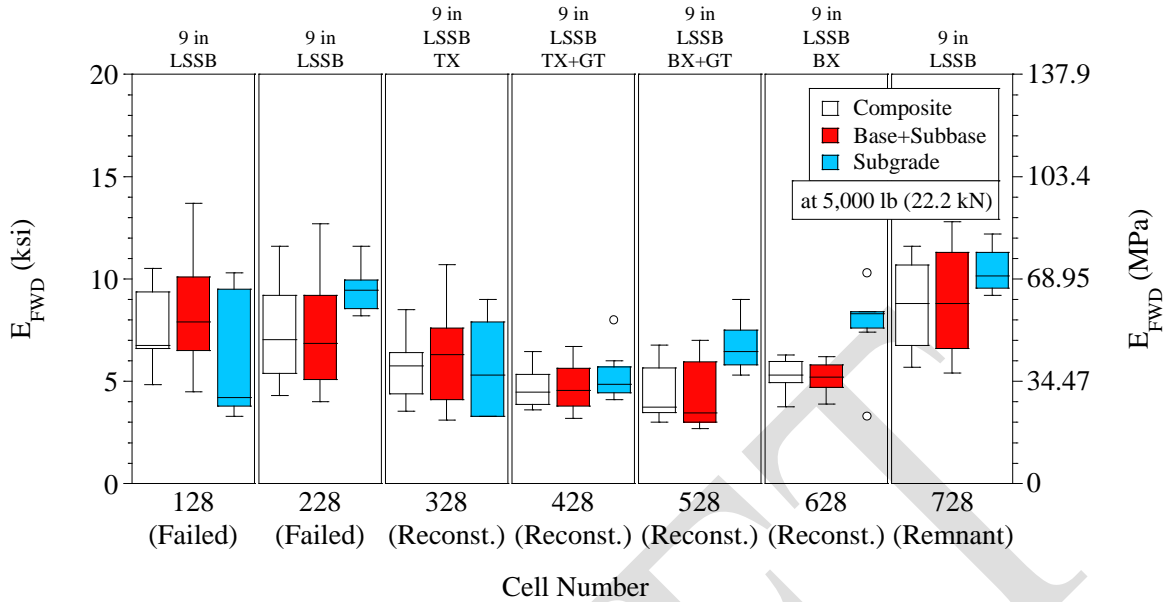


Figure 4.22. FWD elastic moduli of failed, reconstructed, and remnant cells at 5,000 lb (22.2 kN)

2 months after paving, three loading drops ranged between 5,700 lb (25.35 kN) and 12,900 lb (57.38 kN) were applied with increasing load levels. Initially, maximum deflections at three load levels (actual load levels) were compared and no apparent seating effect was observed. Thus, measured deflections were normalized to 6,000 lb (26.7 kN), 9,000 lb (40 kN), and 12,000 lb (53.4 kN) loads and chart showing maximum deflections were plotted based on normalization (Figure 4.23). As seen in Figure 4.23, cells 185, 186, 127, and 227 yielded similar maximum deflections at each load level. Cells 188 and 189 showed intermediate maximum deflection values. Cells constructed with 9-in (229-mm) thick LSSB layers (cells 328 to 728) showed the highest maximum deflections compared to other cells.

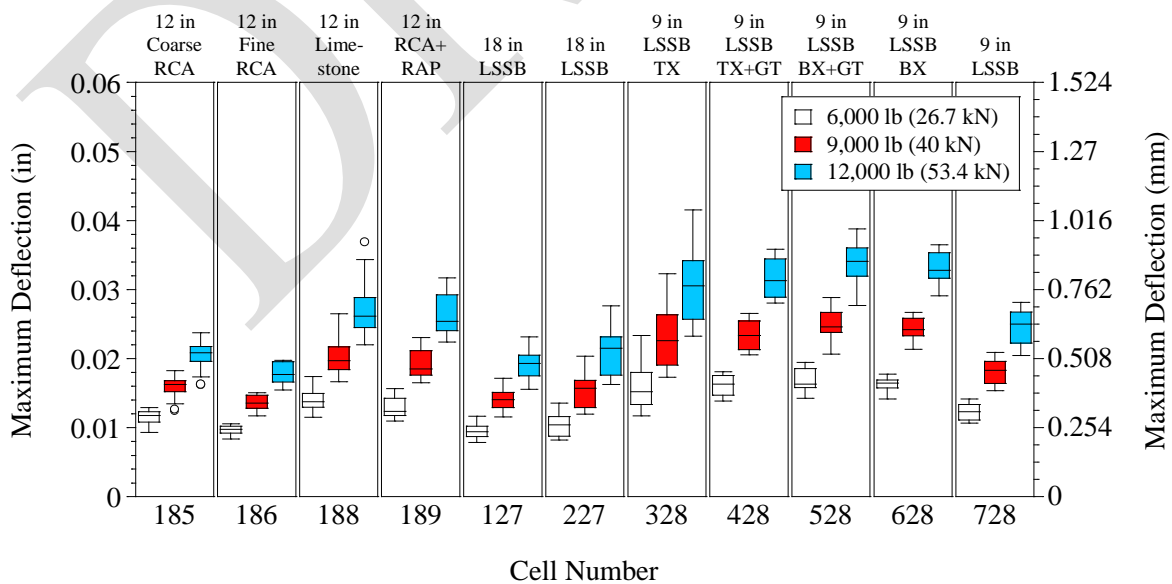


Figure 4.23. Maximum deflections of cells 185 to 728 after paving

Very similar relationships were observed between elastic moduli of cells after paving at 6,000 lb (26.7 kN), 9,000 lb (40 kN), and 12,000 lb (53.4 kN) load levels; therefore, only the elastic moduli of cells at 9,000-lb (40-kN) load is shown in Figure 4.24. Elastic moduli at 6,000 lb (26.7 kN) and 12,000 lb (53.4 kN) load levels are shown in Appendix P (separate charts for subgrade, base+subbase, asphalt, and composite elastic moduli analyses are also provided in Appendix P). While similar maximum deflections (Figure 4.23) and composite elastic moduli (Figure 4.24) were observed in cells 185, 186, 127 and 227, cells 185 and 186 provided relatively higher base+subbase elastic moduli (Figure 4.24). Figure 4.25 provides asphalt elastic moduli of test cells at 9,000 lb (40 kN load level). Although cells 127 and 227 have lower base+subbase moduli than cells 185 and 186 (Figure 4.24), relatively higher asphalt moduli of cells 127 and 227 (Figure 4.25) improved their overall (composite) stiffness values.

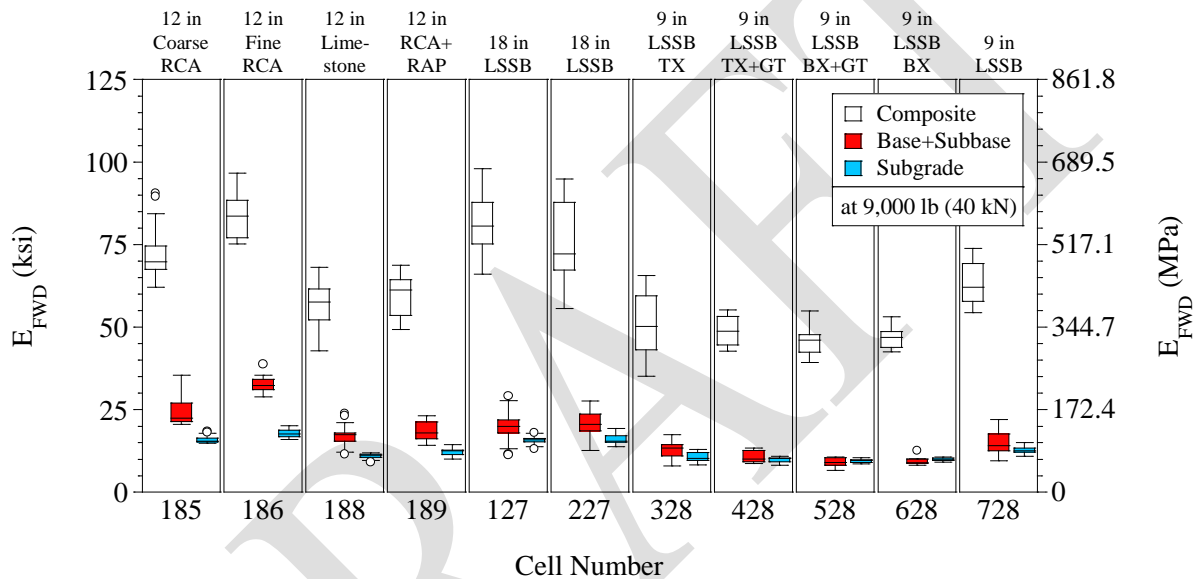


Figure 4.24. FWD elastic moduli of cells 185 to 728 at 9,000 lb (40 kN) after paving

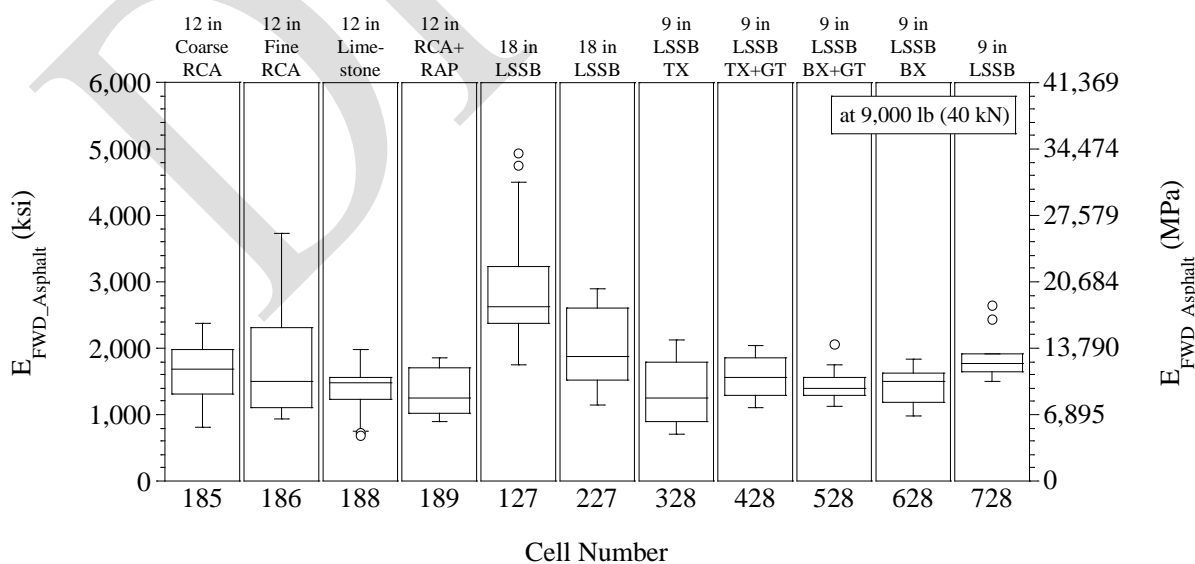


Figure 4.25. Asphalt elastic moduli of cells 185 to 728 at 9,000 lb (40 kN)

5. SUMMARY

The majority of VAs produced annually in the U.S. are used for pavement construction and maintenance. Several reasons such as the depletion of the sources of VAs and local/federal restrictions on their production have increased the price of these materials. This study aims to provide alternative materials such as RCA, RAP, and LSSB materials for replacing VAs. By doing so, the use of natural sources and energy consumption can be reduced, and overall project savings can be provided. To achieve this goal, around 0.4 miles (0.64 km) of the MnROAD LVR operated by the MnDOT was dedicated for eleven test cells constructed with RAB or LSSB layers. Four of the cells were constructed with 12-in (305-mm) thick RAB layers, two of them were constructed with 18-in (457-mm) thick LSSB layers, and five of them were constructed with 9-in (229-mm) thick LSSB layers (with or without geosynthetics). All of the cells except for two cells (cells 185 and 186) were constructed over similar subgrade soils and the same paving material was applied after the completion of the base layers. A systematic approach was provided by constructing all these cells side-by-side to obtain a more consistent performance evaluation process.

Several field tests such as in-situ density and moisture content (with NDG), DCP, LWD, IC, and FWD tests, and GPT were conducted along with systematic construction inspections including tracking the number of passes for compaction and measuring the layer thicknesses. Temperature and moisture sensors, dynamic pressure cells, geophones, and dynamic strain gauges were installed at various depths and offsets in select cells for continuous data acquisition. In addition, air temperature, relative humidity and precipitation measurement are taken every hour by two external weather stations located at the MnROAD LVR. In addition to these monitoring systems, surface characteristics of paved surfaces are evaluated by relevant equipment periodically.

The observations made during construction show that there were some challenges with constructing LSSB layers in general. However, solutions were found in a short span of time and required modifications were made to the design of LSSB layers. In the end, construction of all test cells was completed successfully. DCP, LWD, IC, and FWD data collected during construction showed that two cells constructed with coarse RCA and fine RCA base layers (cells 185 and 186, respectively) performed better (lower DCPI, higher elastic and resilient moduli, and lower deflections) than other cells. Cells constructed with 18-in (427-mm) thick LSSB layers (cells 127 and 227) showed relatively higher moduli and lower deflections than cells constructed with 9-in (229-mm) thick LSSB layers (cells 328 to 728) which indicated that they performed better than cells constructed with thinner LSSB layers. In fact, the lowest performances (higher DCPI, lower moduli, and higher deflections) were observed in cells constructed with 9-in (229-mm) thick LSSB layers (cells 328 to 728).

Evaluation of failed, reconstructed, and remnant cells showed that no superior performance was observed in reconstructed test cells compared to the failed ones. During construction, using geosynthetics between 9-in thick LSSB layers and clayey subgrade soils mitigated rutting and subgrade soil pumping under construction traffic. More analyses will be performed as monitoring continues to observe the long-term performance of each cell and the effects of geosynthetics.

6. REFERENCES

- AASHTO, M 145-91 (2008). Classification of soil and soil-aggregate mixtures for highway construction purposes, American Association of State Highway and Transportation Officials Washington, D.C.
- Abdelrahman, M., Alam, T., and Zollars, J. (2010). Performance of high recycled asphalt pavement (RAP) content as base layer in flexible pavement. *The Journal of Solid Waste Technology and Management*, 36(3), 131-142.
- ACPA (2010). Why Recycle Concrete Pavements? TS043.1P. American Concrete Paving Association, Skokie, IL. <http://1204075.sites.myregisteredsite.com/downloads/TS/EB043P/TS043.1P.pdf>.
- ASTM D6951/D6951M-18 (2018). Standard Test Method for Use of the Dynamic Cone Penetrometer in Shallow Pavement Applications, ASTM International, West Conshohocken, PA.
- ASTM D5283-07 (2015). Standard Test Method for Measuring Deflections with a Light Weight Deflectometer (LWD), ASTM International, West Conshohocken, PA.
- Baladi, G., Thottempudi, A., and Dawson, T. A. (2011). Backcalculation of Unbound Granular Layer Moduli (No. RC-1548).
- Bennert, T., Papp Jr, W., Maher, A., and Gucunski, N. (2000). Utilization of construction and demolition debris under traffic-type loading in base and subbase applications. *Transportation research record: journal of the transportation research board*, (1714), 33-39.
- Bestgen, J. O., Hatipoglu, M., Cetin, B., and Aydilek, A. H. (2016). Mechanical and environmental suitability of recycled concrete aggregate as a highway base material. *Journal of Materials in Civil Engineering*, 28(9), 04016067.
- Cetin, A., Kaya, Z., Cetin, B., and Aydilek, A. H. (2014). Influence of laboratory compaction method on mechanical and hydraulic characteristics of unbound granular base materials. *Road Materials and Pavement Design*, 15(1), 220-235.
- Chatti, K., Kutay, M. E., Lajnef, N., Zaabar, I., Varma, S., and Lee, H. S. (2017). Enhanced Analysis of Falling Weight Deflectometer Data for Use with Mechanistic-Empirical Flexible Pavement Design and Analysis and Recommendations for Improvements to Falling Weight Deflectometers (No. FHWA-HRT-15-063). Turner-Fairbank Highway Research Center.
- Copeland, A. (2011). Reclaimed Asphalt Pavement in Asphalt Mixtures: State of the Practice. Publication FHWA-HRT-11-021. FHWA, U.S. Department of Transportation.
- Cosentino, P. J., and Kalajian, E. H. (2001). Developing Specifications for Using Recycled Asphalt Pavement as Base, Subbase, or General Fill Materials: Final Report. State Materials Office, Florida Department of Transportation, Gainesville, FL.
- Cosentino, P. J., Kalajian, E. H., Shieh, C. S., Mathurin, W. J. K., Gomez, F. A., Cleary, E. D., and Treeratkoorn, A. (2003). Developing Specifications for Using Recycled Asphalt Pavement as Base, Subbase, or General Fill Materials, Phase II: Final Report. Report FL/DOT/RMC/06650-7754. Florida Department of Transportation, Tallahassee, FL.
- Edil, T. (2011). Specifications and recommendations for recycled materials used as unbound base course, Recycled Materials Resource Center, Univ. of Wisconsin-Madison, Madison, WI.
- Edil, T. B., and Cetin, B. (2015). Freeze-thaw performance of chemically stabilized natural and recycled highway materials. *Sciences in Cold and Arid Regions*, 7(5), 0482-0491.

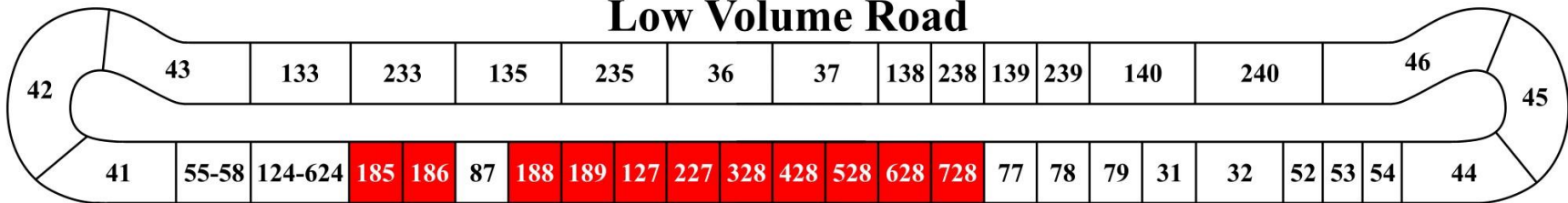
- Edil, T. B., Tinjum, J. M., and Benson, C. H. (2012). Recycled Unbound Materials. Report No. 2012-35. Minnesota Department of Transportation. St. Paul, MN.
- Garach, L., López, M., Agrela, F., Ordóñez, J., Alegre, J., and Moya, J. A. (2015). Improvement of Bearing Capacity in Recycled Aggregates Suitable for Use as Unbound Road Sub-Base. *Materials*, 8(12), 8804-8816.
- Gonzalez, G. P., and Moo-Young, H. K. (2004). Transportation applications of recycled concrete aggregate. FHWA State of the Practice National Review.
- Haider, I., Kaya, Z., Cetin, A., Hatipoglu, M., Cetin, B., and Aydilek, A. H. (2014). Drainage and mechanical behavior of highway base materials. *Journal of Irrigation and Drainage Engineering*, 140(6), 04014012.
- Jayakody, S., Gallage, C., and Kumar, A. (2012). Assessment of Recycled Concrete Aggregate for Road Base and Sub-Base. Proceedings of the Second International Conference on Geotechnique, Construction Materials and Environment, Kuala Lumpur, Malaysia, 2012.
- Kazmee, H., and Tutumluer, E. (2015). Evaluation of Aggregate Subgrade Materials Used as Pavement Subgrade/Granular Subbase. Report FHWA-ICT-15-013. Illinois Department of Transportation, Springfield, IL.
- Kazmee, H., Mishra, D., and Tutumluer, E. (2015). Sustainable Alternatives in Low Volume Road Base Course Applications Evaluated through Accelerated Pavement Testing. Proceedings of the 2015 International Foundations Congress and Equipment Exposition, Reston, VA.
- Kazmee, H., Tutumluer, E., and Beshears, S. (2016). Pavement working platforms constructed with large-size unconventional aggregates. *Transportation Research Record: Journal of the Transportation Research Board*, (2578), 1-11.
- Kuo, S. S., Mahgoub, H., and Nazef, A. (2002). Investigation of recycled concrete made with limestone aggregate for a base course in flexible pavement. *Transportation Research Record: Journal of the Transportation Research Board*, (1787), 99-108.
- Lee, J., Edil, T., Tinjum, J., and Benson, C. (2010). Quantitative assessment of environmental and economic benefits of recycled materials in highway construction. *Transportation Research Record: Journal of the Transportation Research Board*, (2158), 138-142.
- Little, D. N., and Nair, S. (2009). NCHRP Web-Only Document 144: Recommended Practice for Stabilization of Subgrade Soils and Base Materials, Transportation Research Board of the National Academies, Washington, D.C.
- Liu, W., and Scullion, T. (2001). MODULUS 6.0 for windows: User's manual (No. FHWA/TX-05/0-1869-2). Texas Transportation Institute, Texas A&M University System.
- LRRB (2016). Recycled Materials in Unbound Aggregate Base Layers in Minnesota. Transportation Research Synthesis (TRS 1604). Local Road Research Board, Minnesota Department of Transportation.
- MacGregor, J., Highter, W., and DeGroot, D. (1999). Structural numbers for reclaimed asphalt pavement base and subbase course mixes. *Transportation Research Record: Journal of the Transportation Research Board*, (1687), 22-28.
- MnDOT (2009). Density – Nuclear Density Gauge, <https://www.dot.state.mn.us/mnroad/instrumentation/pdfs/nucleardensity.pdf>.
- MnDOT (2013). MnROAD Semi Tractor Trailer, [https://www.dot.state.mn.us/mnroad/data/pdfs/MnROADSemiDescriptions\(March%202013\).pdf](https://www.dot.state.mn.us/mnroad/data/pdfs/MnROADSemiDescriptions(March%202013).pdf).
- MnDOT (2014a). Building Temperature Sensing Arrays (Thermocouple Trees), [http://www.dot.state.mn.us/mnroad/pdfs/BuildingTemperatureSensors-TCTree\(April2014\).pdf](http://www.dot.state.mn.us/mnroad/pdfs/BuildingTemperatureSensors-TCTree(April2014).pdf).

- MnDOT (2014b). Moisture Content – EW (EC, ET), http://www.dot.state.mn.us/mnroad/data/pdfs/Base_Moisture_EC_EW_ET.pdf.
- MnDOT (2018). Standard Specifications for Construction (2018 Edition). Minnesota Department of Transportation, St. Paul, MN.
- Newcomb, D. E., Van Deusen, D. A., Jiang, Y., and Mahoney, J. P. (1995). Considerations of Saturated Soil Conditions in Backcalculation of Pavement Layer Moduli. Transportation Research Record, (1473)
- Nokkaew, K., Tinjum, J. M., and Benson, C. H. (2012). Hydraulic properties of recycled asphalt pavement and recycled concrete aggregate. In GeoCongress 2012: State of the Art and Practice in Geotechnical Engineering (pp. 1476-1485).
- Rahardjo, H., Vilayvong, K., and Leong, E. C. (2010). Water characteristic curves of recycled materials. Geotechnical Testing Journal, 34(1), 89-96.
- Rohde, G. T., Smith, R. E., and Scullion, T. (1992). Pavement deflection analysis on sections where the subgrade vary in stiffness with depth. In International Conference on Asphalt Pavements, 7th, 1992, Nottingham, United Kingdom (Vol. 3).
- Rosa, M., Cetin, B., Edil, T.B., and Benson, C.H. (2017), “Freeze-Thaw Performance of Fly Ash-Stabilized Materials and Recycled Pavement Materials. Journal of Materials in Civil Engineering, 2017. 29(6): 04017015.
- Schuettelpelz, C. C., Fratta, D., and Edil, T. B. (2010). Mechanistic Corrections for Determining the Resilient Modulus of Base Course Materials Based on Elastic Wave Measurements. Journal of Geotechnical and Geoenvironmental Engineering, 136(8), 1086-1094.
- Siekmeier, J., Pinta C., Merth S., Jensen J., Davich P., Camargo F., and Beyer M. (2009). Using the Dynamic Cone Penetrometer and the Lightweight Deflectometer for Construction Quality Assurance. Report MN/RC 2009-12. Minnesota Department of Transportation, St. Paul, MN.
- Stolle, D. F., Guo, P., and Emery, J. J. (2014). Mechanical properties of reclaimed asphalt pavement—natural aggregate blends for granular base. Canadian Journal of Civil Engineering, 41(6), 493-499.
- Tutumluer, E. (2013). Practices for Unbound Aggregate Pavement Layers: A Synthesis of Highway Practice. Transportation Research Board of the National Academies, Washington, DC, Rep. NCHRP Synthesis, 445.
- Tutumluer, E., Huang, H., and Bian, X. (2010). Geogrid-aggregate interlock mechanism investigated through aggregate imaging-based discrete element modeling approach. International Journal of Geomechanics, 12(4), 391-398.
- Tutumluer, E., Xiao, Y., and Wilde, W. J. (2015). Cost-Effective Base Type and Thickness for Long-Life Concrete Pavements. Report No. MN/RC 2015-42. Minnesota Department of Transportation, St. Paul, MN.
- USGS (2018). Mineral Commodity Summaries 2018. U.S. Department of the Interior.
- Uhlmeier, J., Pierce, L., Lovejoy, J., Gribner, M., Mahoney, J., and Olson, G. (2003). Design and construction of rock cap roadways: Case study in Northeast Washington State. Transportation Research Record: Journal of the Transportation Research Board, (1821), 39-46.

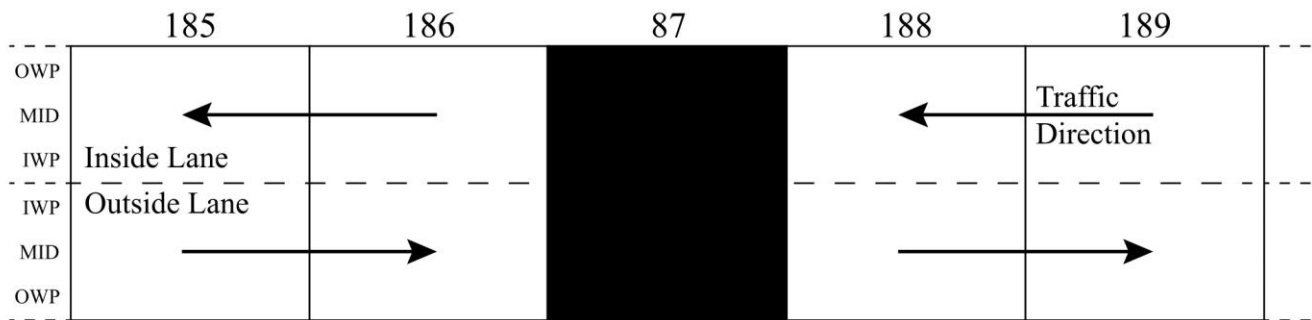
- Van Deusen, D., Burnham, T., Dai, S., Geib, J., Hanson, C., Izevbekhai, B., Johnson, E., Palek, L., Siekmeier, J., Vrtis, M., and Worel, B. (2018). Report on 2017 MnROAD Construction Activities. Report MN/RC 2018-16. Minnesota Department of Transportation, St. Paul, MN.
- Vennapusa, P. K., and White, D. J. (2009). Comparison of light weight deflectometer measurements for pavement foundation materials. *Geotechnical Testing Journal*, 32(3), 1-13.
- Westover, T. M., Labuz, J. F., and Guzina, B. B. (2007). Resilient Modulus Development of Aggregate Base and Subbase Containing Recycled Bituminous and Concrete for 2002 Design Guide and Mn/Pave Pavement Design. Report No. MN/RC-2007-25. Minnesota Department of Transportation, St. Paul, MN.
- White, D. J., and Vennapusa, P. (2017) 2017 MnROAD Unbound Layer Evaluation Using Intelligent Compaction: Ingios Validated Intelligent Compaction (VIC) Results. Report 2017-043. Ingios Geotechnics.
- White, D. J., Vennapusa, P. K., Eichner, D., Gieselman, H., Zhao, L., and Jahren, C. (2010). Rapid, self-contained in-situ permeameter for field QA/QC of pavement base/subbase materials. Iowa State University, Ames, IA.
- White, D. J., Vennapusa, P. K., Suleiman, M. T., and Jahren, C. T. (2007). An In-situ Device for Rapid Determination of Permeability for Granular Bases. *Geotechnical Testing Journal*, 30(4), 282-291.
- William, G. W. (1999). Backcalculation of pavement layers moduli using 3D nonlinear explicit finite element analysis (Doctoral dissertation, West Virginia University Libraries).
- Yohannes, B., Hill, K., and Khazanovich, L. (2009). Mechanistic Modeling of Unbound Granular Materials. Report No. MN/RC 2009-21. Minnesota Department of Transportation, St. Paul, MN.
- Zhao, L. (2011). "In situ Assessment of Support and Drainage for PCC Subbase". Graduate Theses and Dissertations. 10262.
- Zornberg, J. G. (2012). Geosynthetic-reinforced pavement systems. In 5th European Geosynthetics Congress, Valencia, Spain.
- Zornberg, J. G. (2017). Functions and applications of geosynthetics in roadways. *Procedia engineering*, 189, 298-306.

APPENDIX A. TEST CELLS ON THE MNROAD LVR AND ROAD LANES

**MnROAD
Low Volume Road**



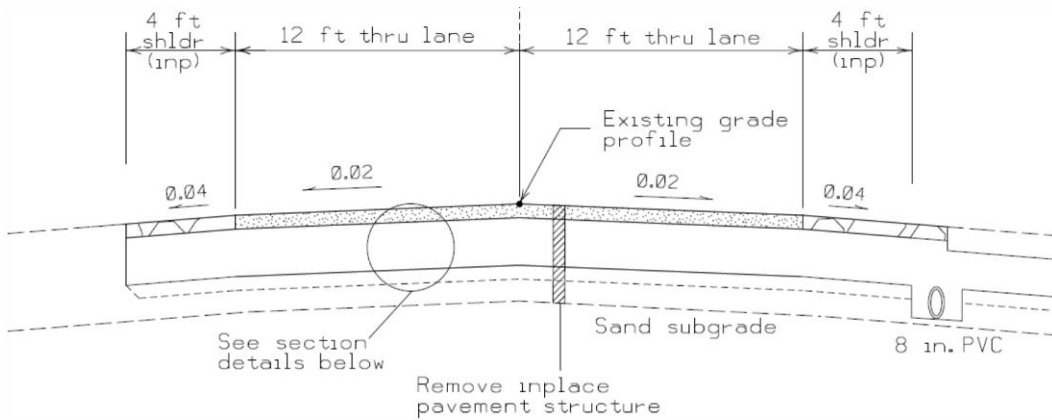
NOTE: Test cells shown in red are related to this project.



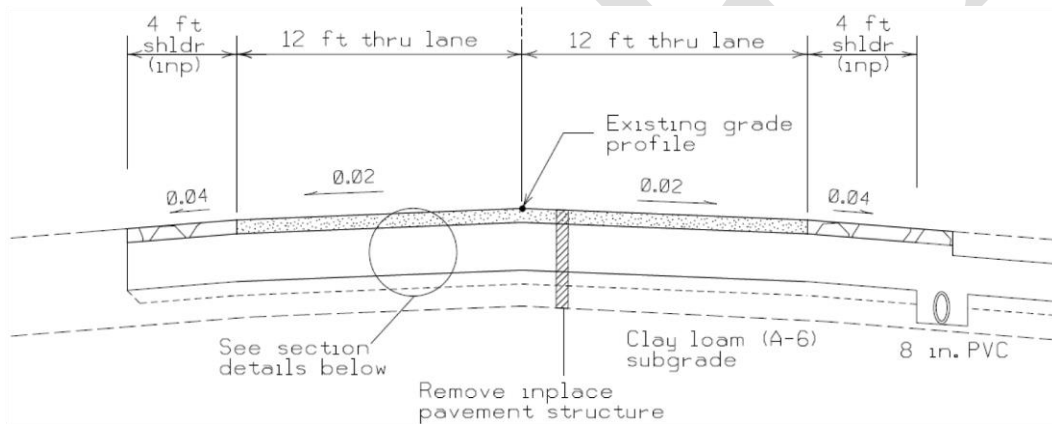
NOTE: OWP: outer wheel path, MID: midline, IWP: inner wheel path

APPENDIX B. CROSS-SECTIONS OF TEST CELLS

Cells 185 and 186 (Van Deusen et al. 2018):

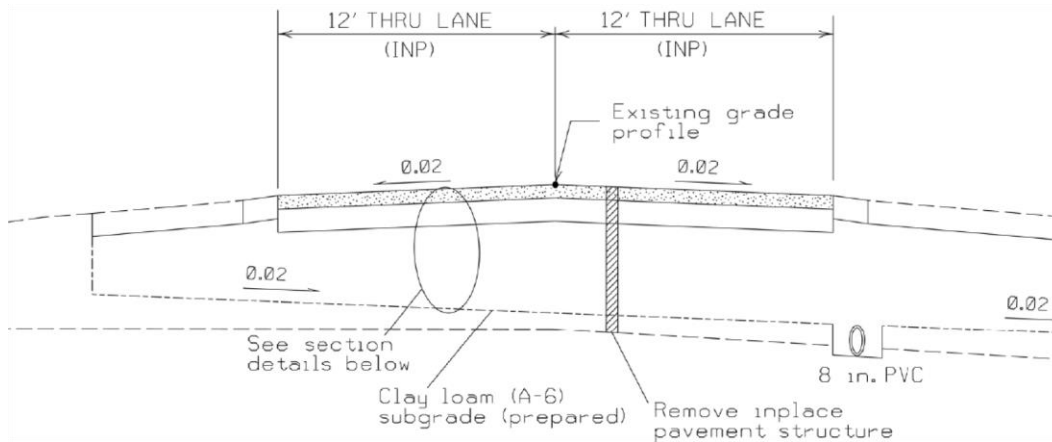


Cells 188 and 189 (Van Deusen et al. 2018):



Recycled Aggregate Base			
185	186	188	189
3.5 in Superpave	3.5 in Superpave	3.5 in Superpave	3.5 in Superpave
12 in Coarse RCA (Class 5Q)	12 in Fine RCA (Class 5)	12 in Limestone (Class 6)	12 in RCA+RAP (Class 6)
3.5 in S. Granular Borrow	3.5 in S. Granular Borrow	3.5 in S. Granular Borrow	3.5 in S. Granular Borrow
Sand	Sand	Clay Loam	Clay Loam

Cells 127, 227, 328, 428, 528, 628, and 728 (Van Deusen et al. 2018):



Large Stone Subbase		Large Stone Subbase with Geosynthetics				
127	227	328	428	528	628	728
3.5 in Superpave	3.5 in Superpave	3.5 in Superpave	3.5 in Superpave	3.5 in Superpave	3.5 in Superpave	3.5 in Superpave
6 in Aggregate (Class 6)	6 in Aggregate (Class 6)	6 in Aggregate (Class 5Q)	6 in Aggregate (Class 5Q)	6 in Aggregate (Class 5Q)	6 in Aggregate (Class 5Q)	6 in Aggregate (Class 5Q)
18 in LSSB (1 lift)	18 in LSSB (1 lift)	9 in LSSB	9 in LSSB	9 in LSSB	9 in LSSB	9 in LSSB
		TX	TX+GT	BX+GT	BX	
		Clay Loam	Clay Loam	Clay Loam	Clay Loam	Clay Loam
Clay Loam	Clay Loam					

APPENDIX C. START AND END STATIONS OF TEST CELLS

	Cell Number	Position	Station	Length (ft)
Recycled Aggregate Base	185	Start	16368	201
		End	16569	
	186	Start	16619	201
		End	16820	
	188	Start	17046	201
		End	17247	
189	Start	17297	200	
	End	17497		
Large Stone Subbase	127	Start	17498	258
		End	17756	
	227	Start	17805	260
		End	18065	
Large Stone Subbase with Geosynthetics	328	Start	18065	109
		End	18174	
	428	Start	18174	109
		End	18283	
	528	Start	18283	108
		End	18391	
	628	Start	18391	113
		End	18504	
	728	Start	18504	131
		End	18635	

APPENDIX D. CONSTRUCTION TIMELINE FOR TEST CELLS

Cells 185, 186, 188, and 189 (Van Deusen et al. 2018):

Activity \ Date	June				July					August				September			
	5	12	19	26	3	10	17	24	31	7	14	21	28	4	11	18	25
Erosion Control	X																
Strip Topsoil																	
Pavement Removal		X	X			X											
Common Excavation						X	X										
Subsurface Drain							X										
Place Conduits and Handholes							X										
Place Risers and Sensors							X			X							
Place Aggregate Base									X								
HMA Paving												X					X

Cells 127, 227, 128, 228, 328, 428, 528, 628, 728 (Van Deusen et al. 2018):

Activity \ Date	June				July					August				September			
	5	12	19	26	3	10	17	24	31	7	14	21	28	4	11	18	25
Erosion Control	X																
Strip Topsoil							X										
Pavement Removal							X										
Common Excavation								X	X	X							
Subsurface Drain										X							
Place Conduits and Handholes																	
Subgrade Preparation											X						
Place Large Aggregate Subbase											X						
Place Risers and Sensors																	
Place Aggregate Base											X						
HMA Paving												X					
Remove Failed Cells (128-228)													X				
Reconstruct Cells (328-628)													X	X			
Final HMA Paving																	X

NOTE: Cells 128 and 228 failed and cells 328, 428, 528, and 628 were reconstructed in place of them. Cell 728 is a remnant from cell 228.

Construction Dates of Each Cell (Van Deusen et al. 2018):

Cell Number	Layer	Subgrade	Base	HMA (1st Layer)	HMA (2nd Layer)
185		7/14/2017	8/10/2017	8/21/2017	9/19/2017
186					
188					
189					
127		8/15/2017	8/19/2017	8/21/2017	9/19/2017
227					
128 (Failed)					
228 (Failed)					
328 (Reconst.)		8/28/2017	8/31/2017	9/19/2017	9/19/2017
428 (Reconst.)					
528 (Reconst.)					
628 (Reconst.)					
728 (Remnant)		8/15/2017	8/19/2017	8/21/2017	9/19/2017

NOTE: Cells 128 and 228 failed and cells 328, 428, 528, and 628 were reconstructed in place of them. Cell 728 is a remnant from cell 228.

APPENDIX E. BASE LAYERS OF CELLS 188 AND 189



(White and Vennapusa 2017)

DRAFT

APPENDIX F. BASE LAYERS OF CELLS 127 AND 227



(White and Vennapusa 2017)

DRAFT

APPENDIX G. CONSTRUCTION OF CELLS 128 AND 228

Placement of LSSB material (White and Vennapusa 2017):



Placement of LSSB material (White and Vennapusa 2017)



Rutting on LSSB layer and subgrade soil pumping under construction traffic (White and Vennapusa 2017):



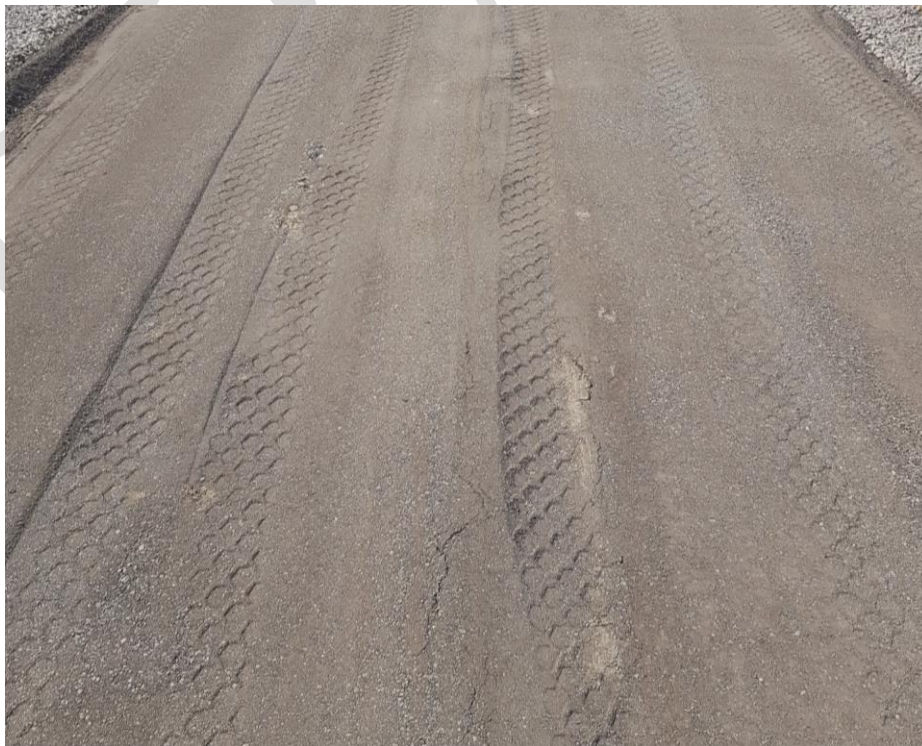
Rutting on LSSB layer and subgrade soil pumping under construction traffic (White and Vennapusa 2017):



Prepared aggregate base layers (White and Vennapusa 2017):



Base layer rutting (White and Vennapusa 2017):



APPENDIX H. GEOSYNTHETICS AND CONSTRUCTION OF CELLS 328, 428, 528, AND 628

Properties of geosynthetics (as reported by manufacturers)

Geosynthetic Type	Property	Test Method	Values
Tensor TriAx TX190L (Triaxial Geogrid)	Rib Pitch ^{a, b}	NA	2.4 in (60 mm)
	Junction Efficiency ^c	ASTM D7737	93%
	Isotropic Stiffness Ratio ^d	NA	0.6
	Radial Stiffness at 0.5% Strain	ASTM D6637	23,989 lb/ft (350 kN/m)
Tensor BX1300 (Biaxial Geogrid)	Aperture Dimensions ^{a, e}	NA	1.8 in (46 mm)
	Minimum Rib Thickness ^{a, e}	NA	0.05 in (1.27 mm)
	Tensile Strength at 5% Strain ^e	ASTM D6637	720 lb/ft (10.5 kN/m)
	Ultimate Tensile Strength ^e	ASTM D6637	1,100 lb/ft (16 kN/m)
SKAPS GT-116 (Needle-Punched Nonwoven Geotextile)	Junction Efficiency ^c	ASTM D7737	93%
	Grab Tensile Strength	ASTM D4632	380 lb (1.690 kN)
	Grab Elongation	ASTM D4632	50%
	Trapezoid Tear Strength	ASTM D4533	145 lb (0.644 kN)
	CBR Puncture Resistance	ASTM D6241	1,080 lb (4.804 kN)
Permittivity ^f	ASTM D4491	0.7 sec ⁻¹	
Apparent Opening Size ^{f, g}	ASTM D4751	0.0059 in (0.150 mm)	

NOTE: NA = not available.

^aNominal dimensions

^bLongitudinal and diagonal

^cLoad transfer capability expressed as a percentage of ultimate tensile strength

^dRatio between the minimum and maximum radial stiffness values at 0.5% strain

^eMachine direction

^fAt time of manufacturing. Results may change after handling.

^gMaximum average roll value.

Compacted aggregate base layers (White and Vennapusa 2017):



DRAFT

APPENDIX I. LOCATIONS OF THE INSTALLED SENSORS

Cells 185, 186, 188, and 189 (Van Deusen et al. 2018):

Cell Number	Sensor	Number	Station	Offset (ft)	Depth from Surface (in)
185	TC	1	16538.51	-6.4	2.8
		2	16538.51	-6.4	3.8
		3	16538.51	-6.4	9.3
		4	16538.51	-6.4	14.8
		5	16538.51	-6.4	15.8
		6	16538.51	-6.4	18.3
		7	16538.51	-6.4	19.3
		8	16538.51	-6.4	23.8
		9	16538.51	-6.4	35.8
		10	16538.51	-6.4	47.8
		11	16538.51	-6.4	59.8
		12	16538.51	-6.4	71.8
	EC	1	16538.81	-5.8	5
		2	16538.81	-5.8	14
		3	16538.81	-5.8	17
		4	16538.81	-5.8	20.5
	PG	1	16526.83	-8.9	23.5
		2	16526.83	-8.9	15
	GP	1			9.5
		2			25
3				43	
4				43	
186	TC	1	16678.52	-6.3	3
		2	16678.52	-6.3	4
		3	16678.52	-6.3	9.5
		4	16678.52	-6.3	15
		5	16678.52	-6.3	16
		6	16678.52	-6.3	18.5
		7	16678.52	-6.3	19.5
		8	16678.52	-6.3	24
		9	16678.52	-6.3	36
		10	16678.52	-6.3	48
		11	16678.52	-6.3	60
		12	16678.52	-6.3	72
	EC	1	16678.91	-5.6	5
		2	16678.91	-5.6	14
		3	16678.91	-5.6	17
		4	16678.91	-5.6	20.5
	PG	1	16667.23	-9.7	27.7
		2	16667.23	-9.7	15
	GP	1			9.5
		2			25
3				43	
4				43	
LE	1	16672.04	-11.3	3	
	2	16672.03	-8.9	3	
TE	1	16667.93	-11.3	3	
	2	16668.00	-8.7	3	
188	TC	1	17111.5	-5.5	3
		2	17111.5	-5.5	4
		3	17111.5	-5.5	9.5
		4	17111.5	-5.5	15
		5	17111.5	-5.5	16
		6	17111.5	-5.5	18.5
		7	17111.5	-5.5	19.5
		8	17111.5	-5.5	24
		9	17111.5	-5.5	36
		10	17111.5	-5.5	48
		11	17111.5	-5.5	60
		12	17111.5	-5.5	72
	EC	1	17111.8	-4.8	5
		2	17111.8	-4.8	14
		3	17111.8	-4.8	17
		4	17111.8	-4.8	20.5
	PG	1	17105.9	-8.9	20.1
		2	17105.9	-8.9	15
	GP	1			9.5
		2			25
3				43	
4				43	
LE	1	17110.9	-11.2	3	
	2	17110.9	-8.8	3	
TE	1	17107	-11.3	3	
	2	17107.1	-8.8	3	
189	TC	1	17306.1	-5.3	3
		2	17306.1	-5.3	4
		3	17306.1	-5.3	9.5
		4	17306.1	-5.3	15
		5	17306.1	-5.3	16
		6	17306.1	-5.3	18.5
		7	17306.1	-5.3	19.5
		8	17306.1	-5.3	24
		9	17306.1	-5.3	36
		10	17306.1	-5.3	48
		11	17306.1	-5.3	60
		12	17306.1	-5.3	72
	EC	1	17306.2	-4.7	5
		2	17306.2	-4.7	14
		3	17306.2	-4.7	17
		4	17306.2	-4.7	20.5
	PG	1	17287.1	-9.2	15
		2	17287.1	-9.2	28
	GP	1			9.5
		2			25
3				43	
4				43	

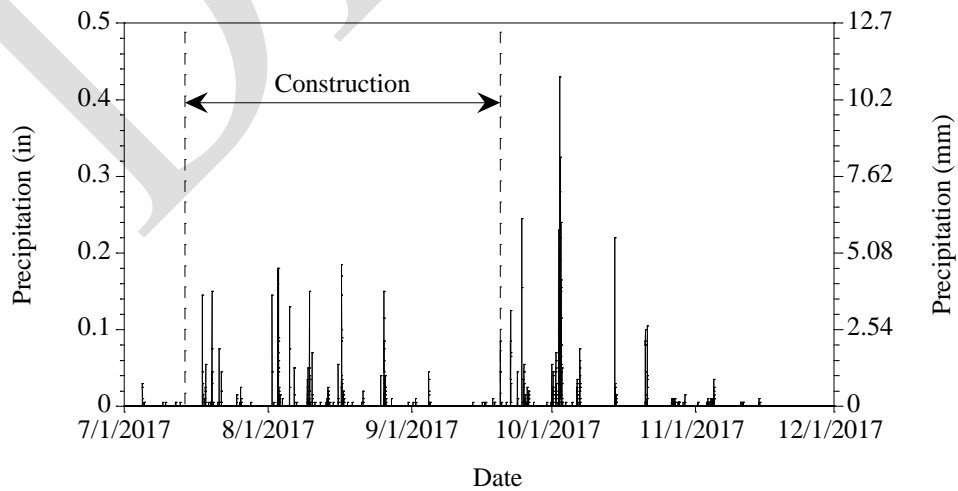
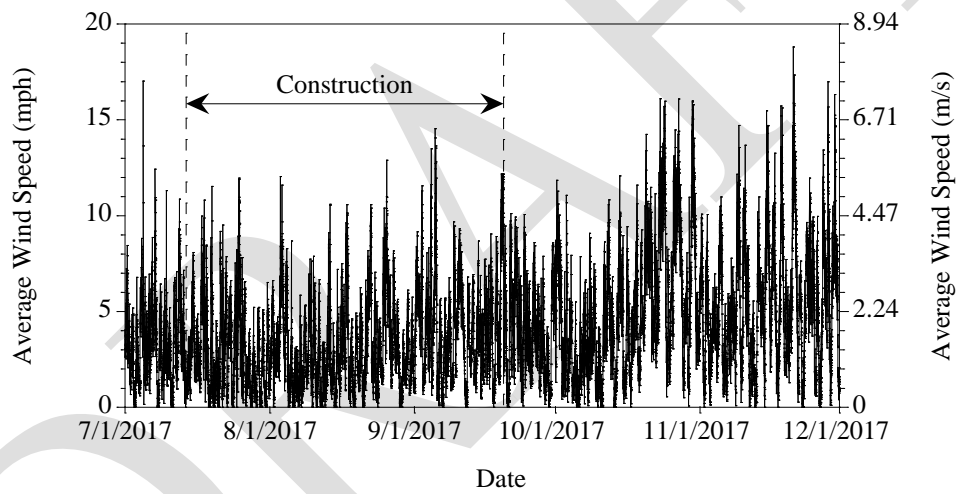
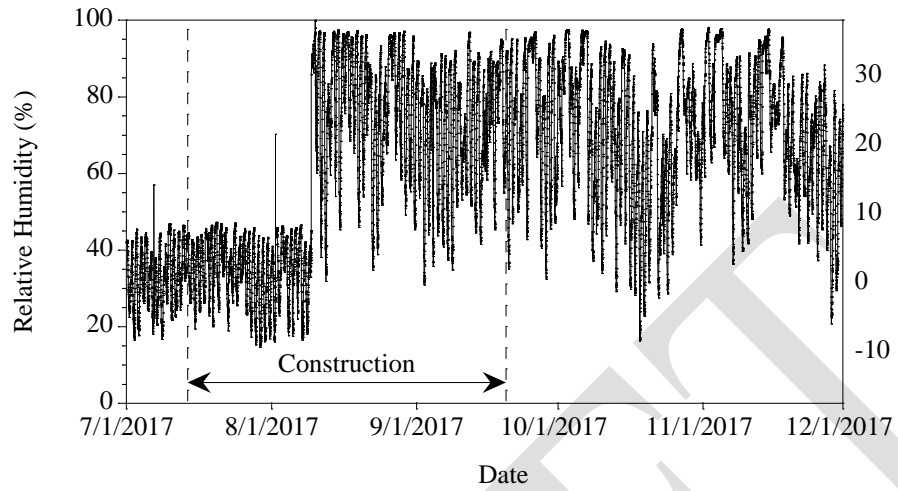
Cells 127 and 728 (Van Deusen et al. 2018):

Cell Number	Sensor	Number	Station	Offset (ft)	Depth from Surface (in)
127	TC	1	17569	-11.5	3
		2	17569	-11.5	4
		3	17569	-11.5	6.5
		4	17569	-11.5	9
		5	17569	-11.5	10
		6	17569	-11.5	12
		7	17569	-11.5	18
		8	17569	-11.5	24
		9	17569	-11.5	36
		10	17569	-11.5	48
		11	17569	-11.5	60
		12	17569	-11.5	72
	EC	1	17569	-11	6.5
		2	17569	-11	29
3		17569	-11	36	
PG	1	17595.1	-8.6	8.5	
	2	17605	-8.5	8.5	

TC = Thermocouple
 EC = Moisture probe
 PG = Dynamic pressure cell
 GP = Geophone
 LE = Longitudinal dynamic strain gauge
 TE = Transverse dynamic strain gauge

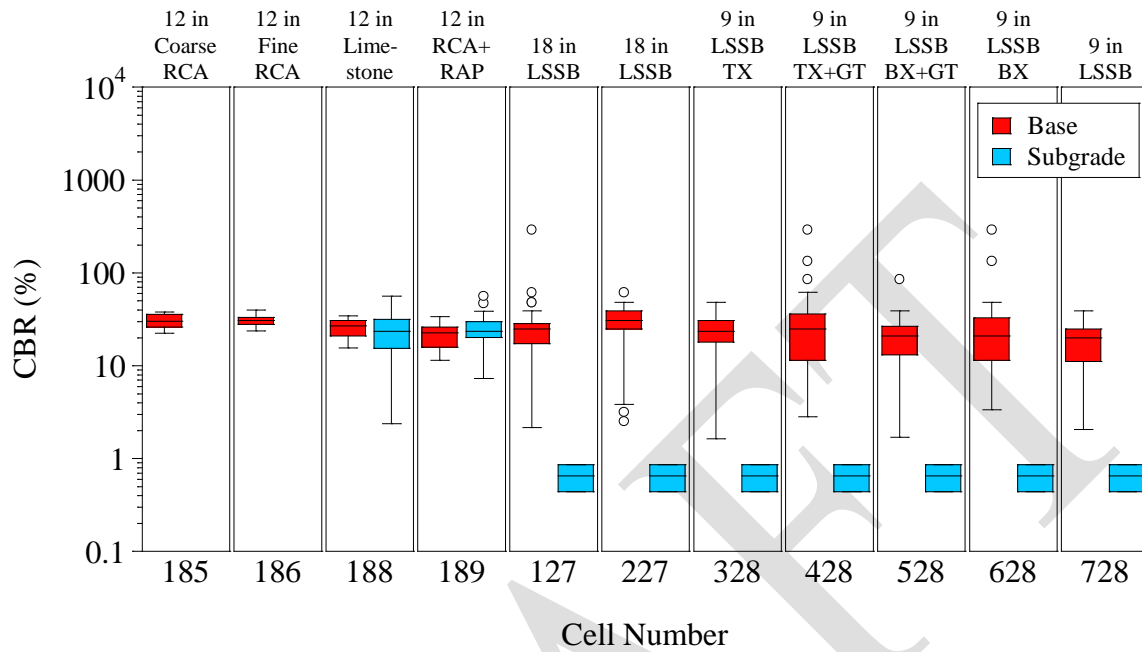
Cell Number	Sensor	Number	Station	Offset (ft)	Depth from Surface (in)
728	TC	1	18544.1	-11.6	3
		2	18544.1	-11.6	4
		3	18544.1	-11.6	6.5
		4	18544.1	-11.6	9
		5	18544.1	-11.6	10
		6	18544.1	-11.6	14
		7	18544.1	-11.6	18.5
		8	18544.1	-11.6	24
		9	18544.1	-11.6	36
		10	18544.1	-11.6	48
		11	18544.1	-11.6	60
		12	18544.1	-11.6	72
		13	18544.1	-11.9	0.3
		14	18544.1	-11.9	1
		15	18544.1	-11.9	2
		16	18544.1	-11.9	3
	EC	1	18544	-11	8.5
		2	18544	-11	19.5
		3	18544	-11	24
		4	18544	-11	36
	PG	1	18505.2	-8.4	8.5
		2	18515.1	-8.4	8.5
	LE	1	18511.9	-11.3	3
		2	18512	-8.7	3
	TE	1	18508	-11.2	3
		2	18508.1	-8.8	3

APPENDIX J. RELATIVE HUMIDITY, AVERAGE WIND SPEED, AND PRECIPITATION DATA

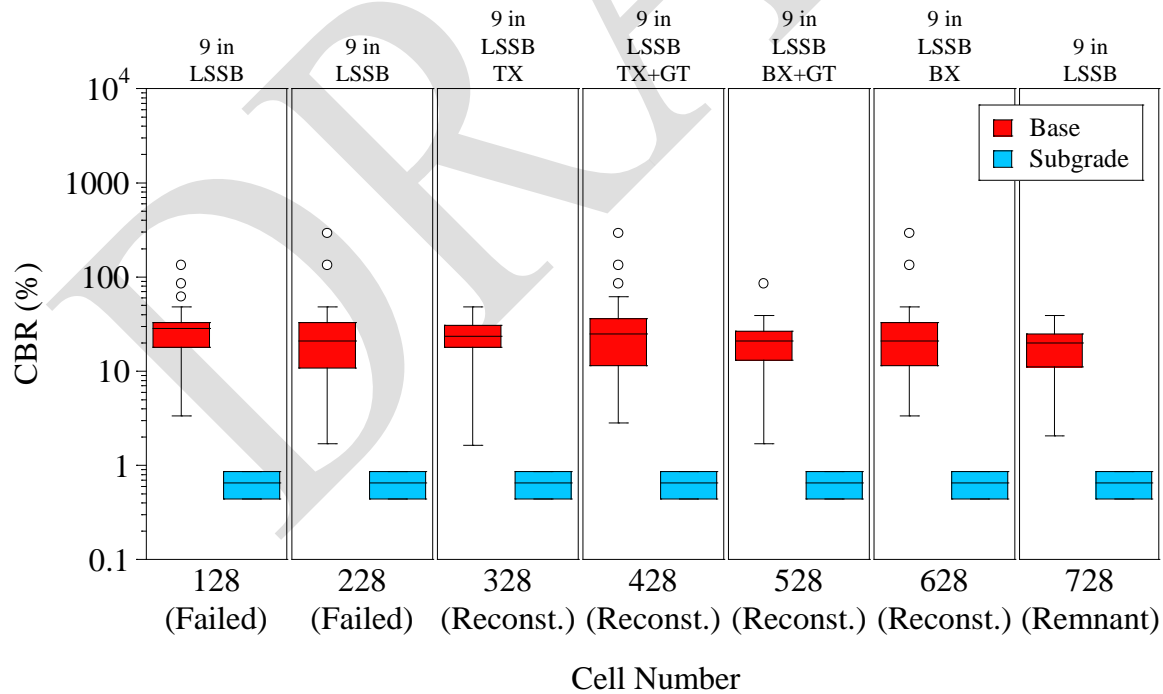


APPENDIX K. CBR VALUES ESTIMATED FROM DCP TEST DATA

CBR values of all test cells:

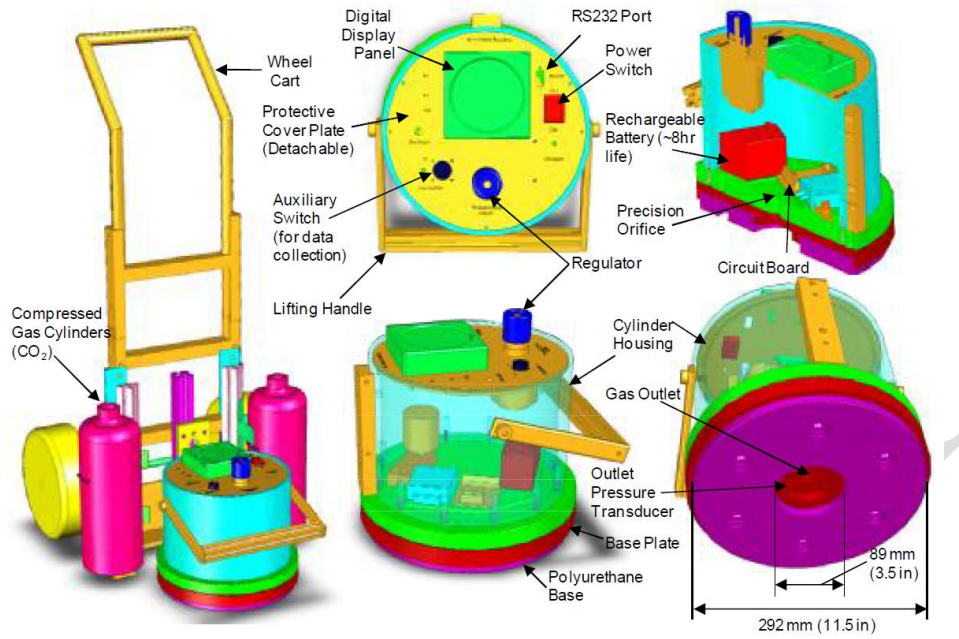


CBR values of failed (cells 128 and 228) and reconstructed (cells 328 to 628) test cells:



APPENDIX L. GPT EQUIPMENT AND TESTED SURFACE TEXTURES

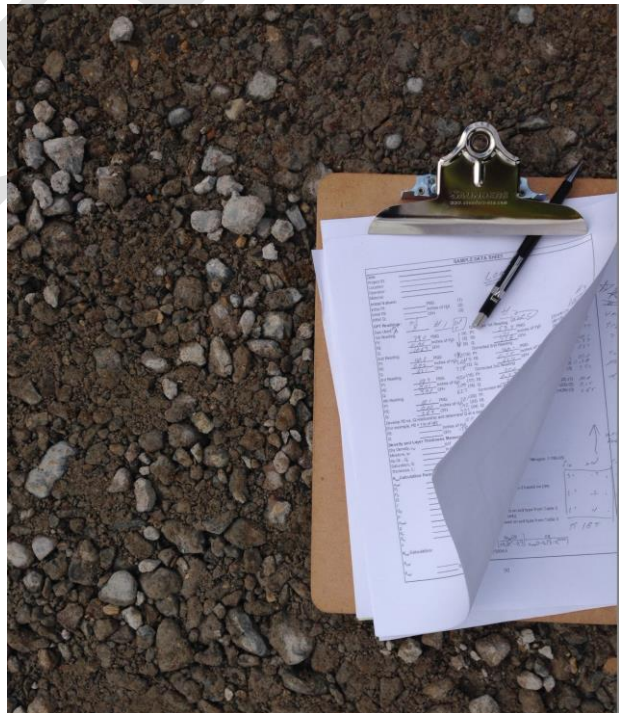
GPT equipment (White et al. 2010):



Fine surface texture



Medium surface texture



Coarse surface texture



APPENDIX M. INTELLIGENT COMPACTION AND ITS CALIBRATION

APLT test system at the MnROAD LVR (White and Vennapusa 2017):



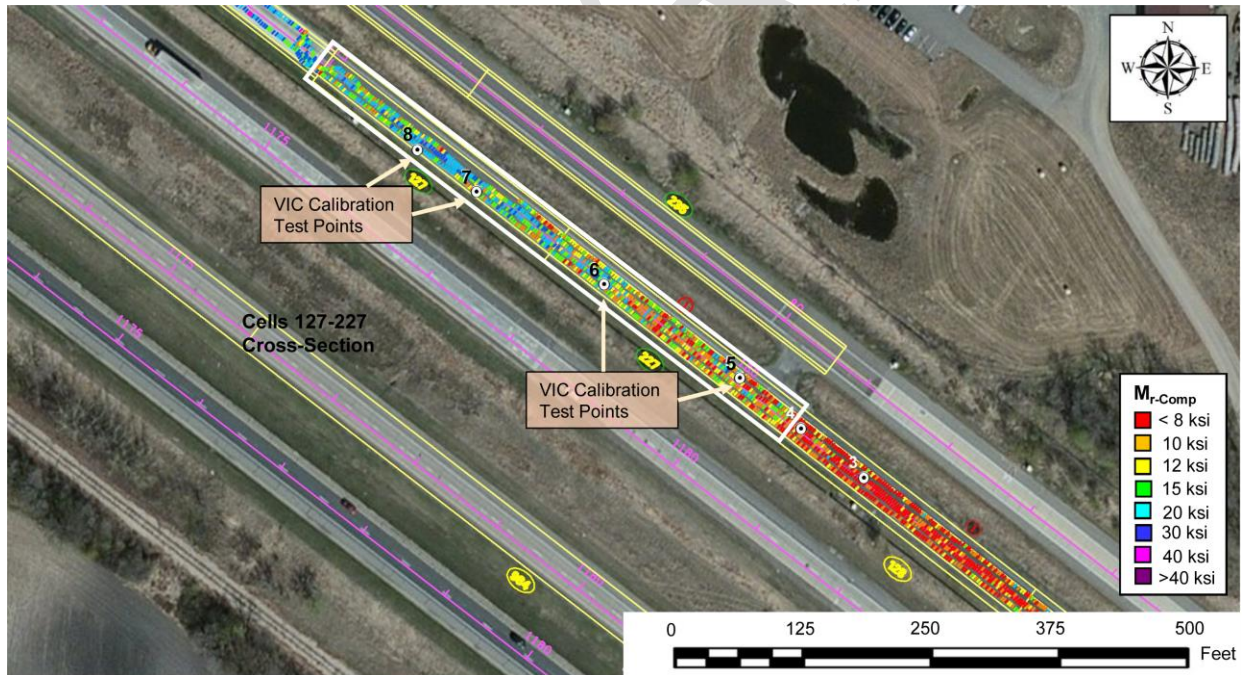
APLT test setup and deflection basin measurement kit with center plate (White and Vennapusa 2017):



Caterpillar CS56 vibratory smooth drum roller outfitted with Ingios VIC system and RTK-GPS (White and Vennapusa 2017):

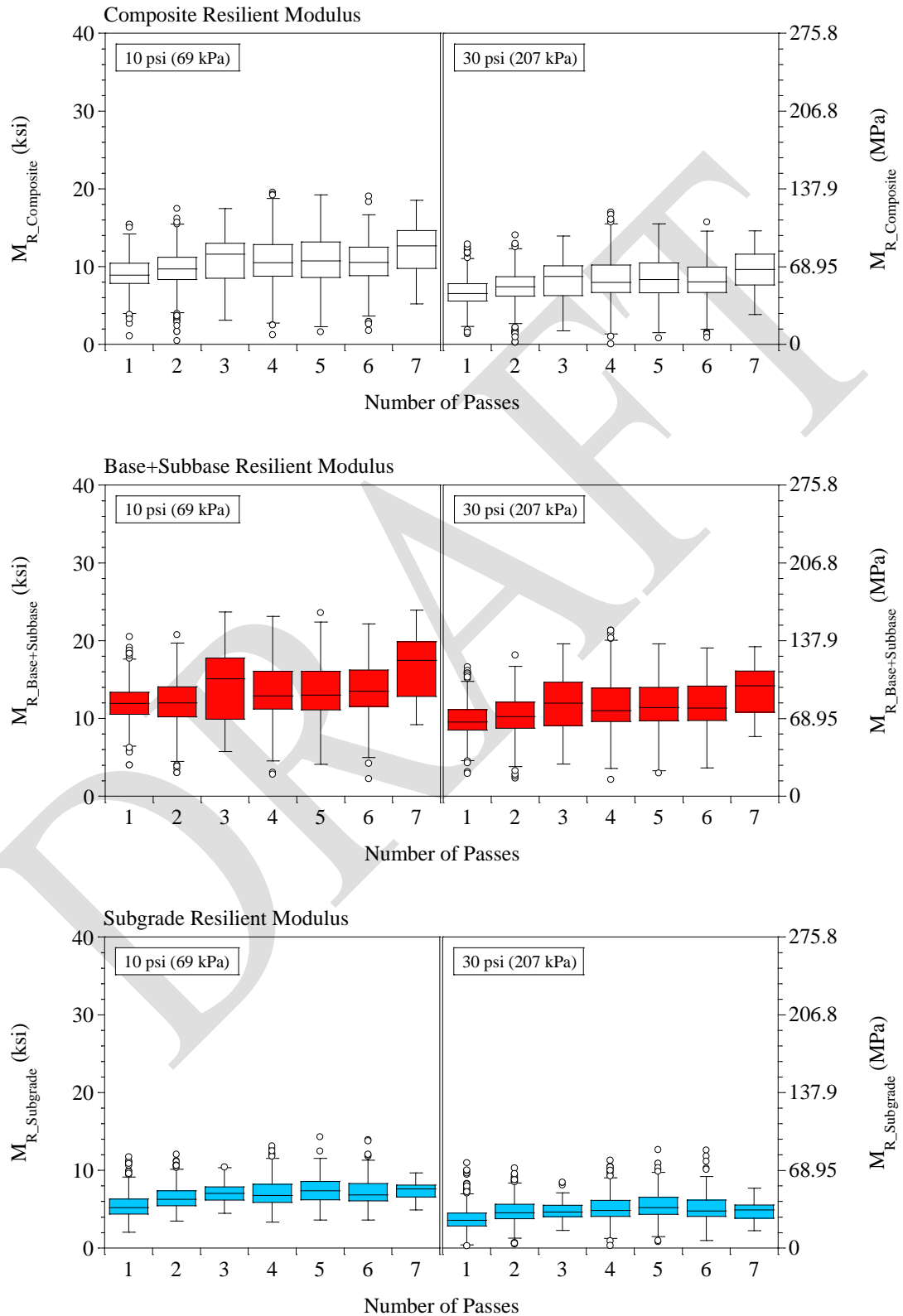


IC mapping for cells 127 and 227 (White and Vennapusa 2017):

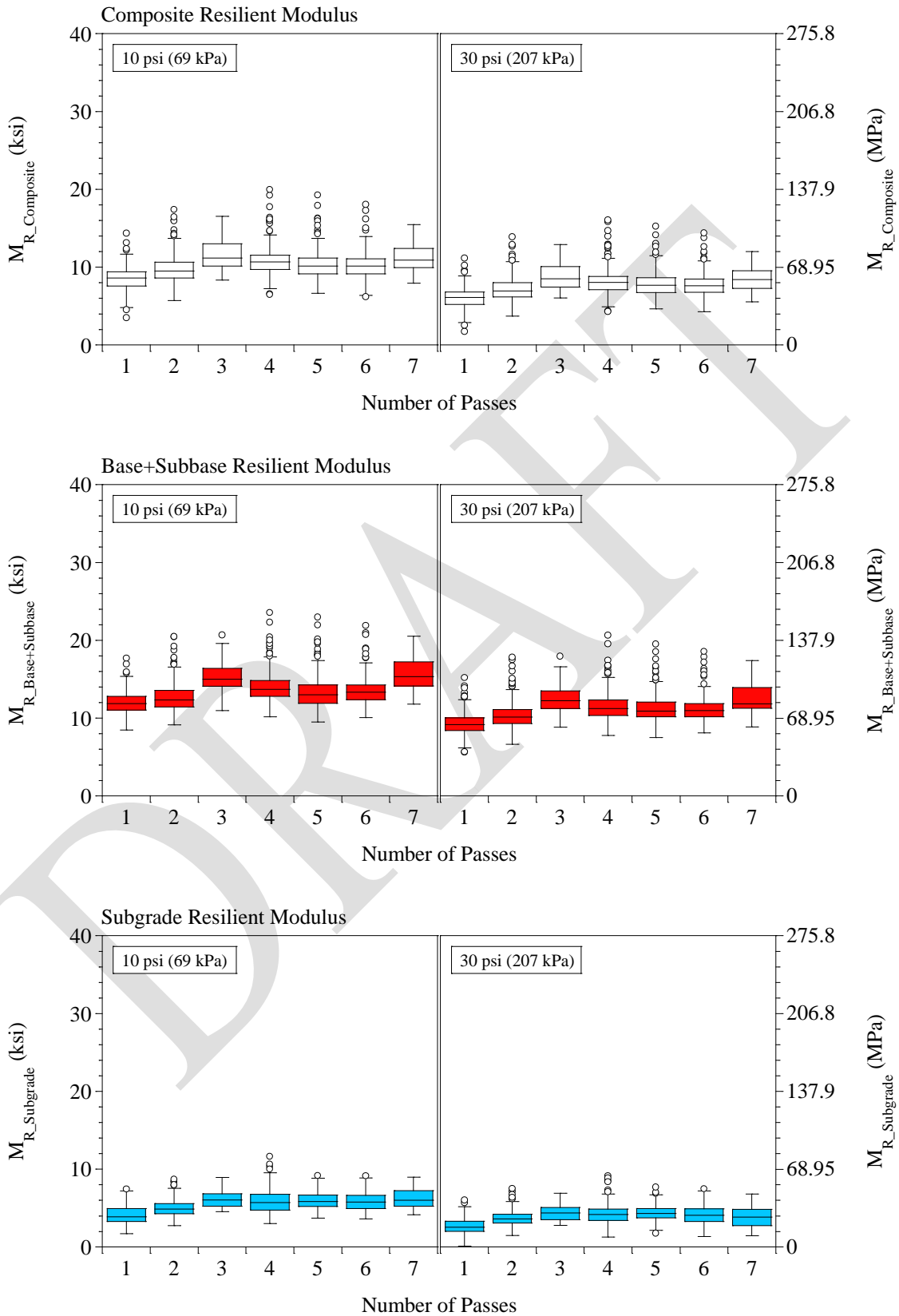


APPENDIX N. RESILIENT MODULI OF RECONSTRUCTED CELLS AT EACH PASS

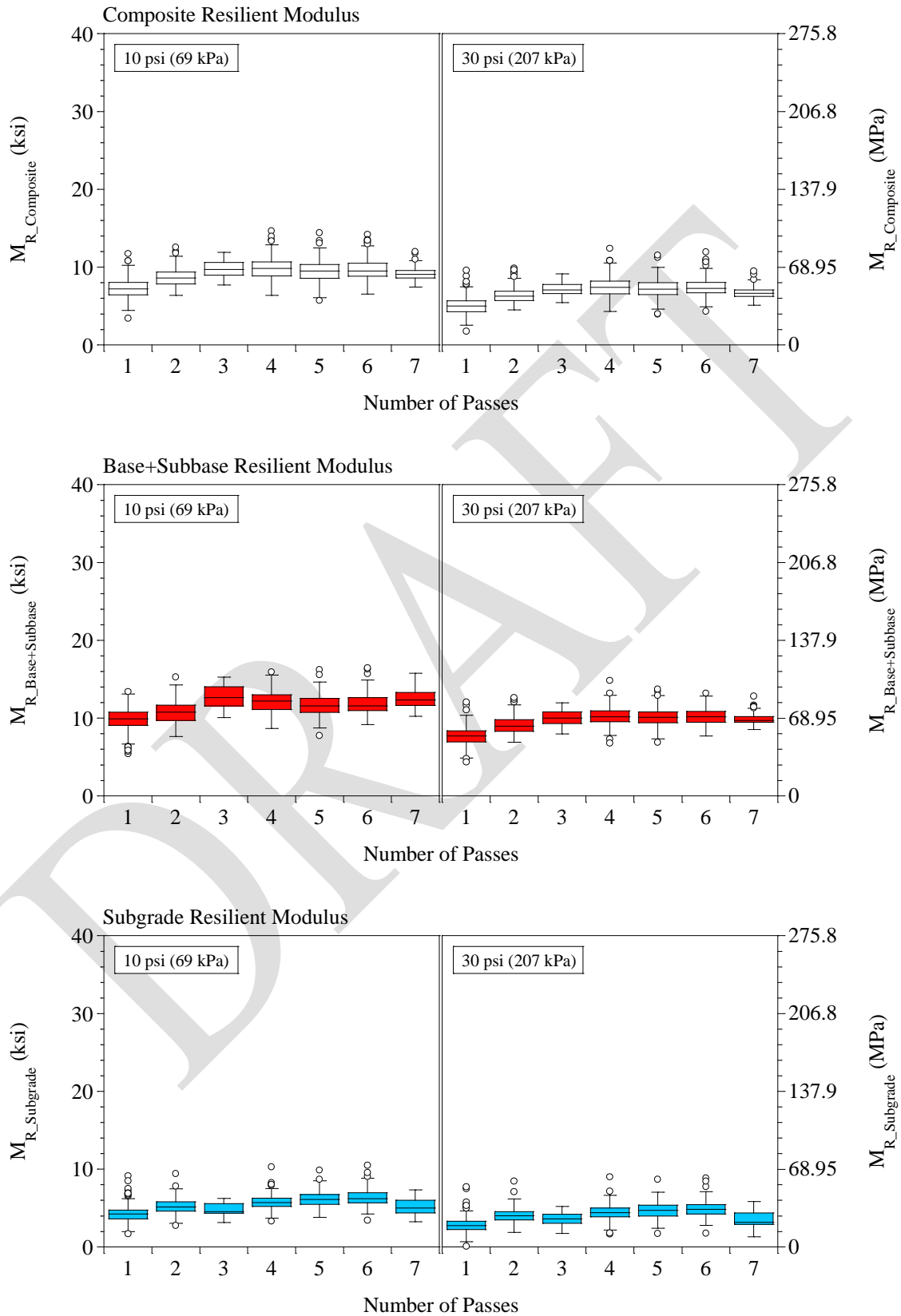
Cell 328:



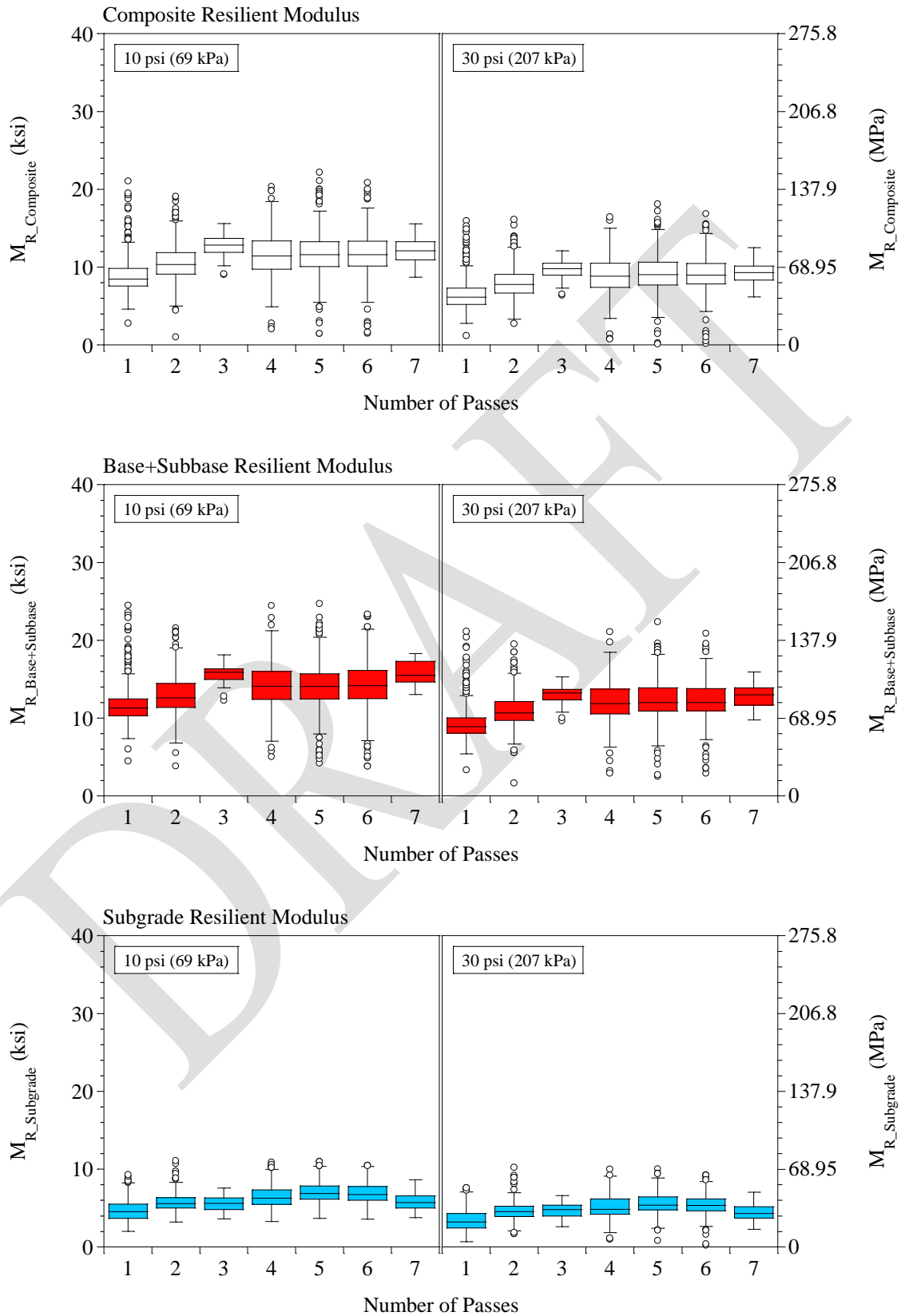
Cell 428:



Cell 528:



Cell 628:



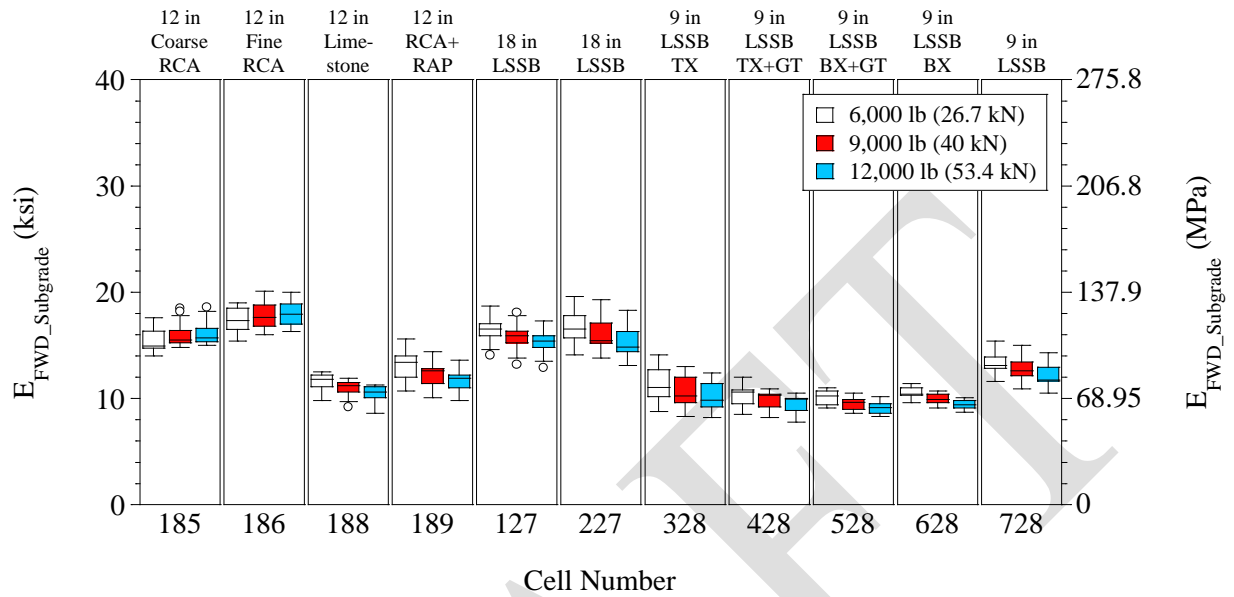
APPENDIX O. FWD TESTING EQUIPMENT

Trailer-mounted Dynatest Model 8002 FWD device:

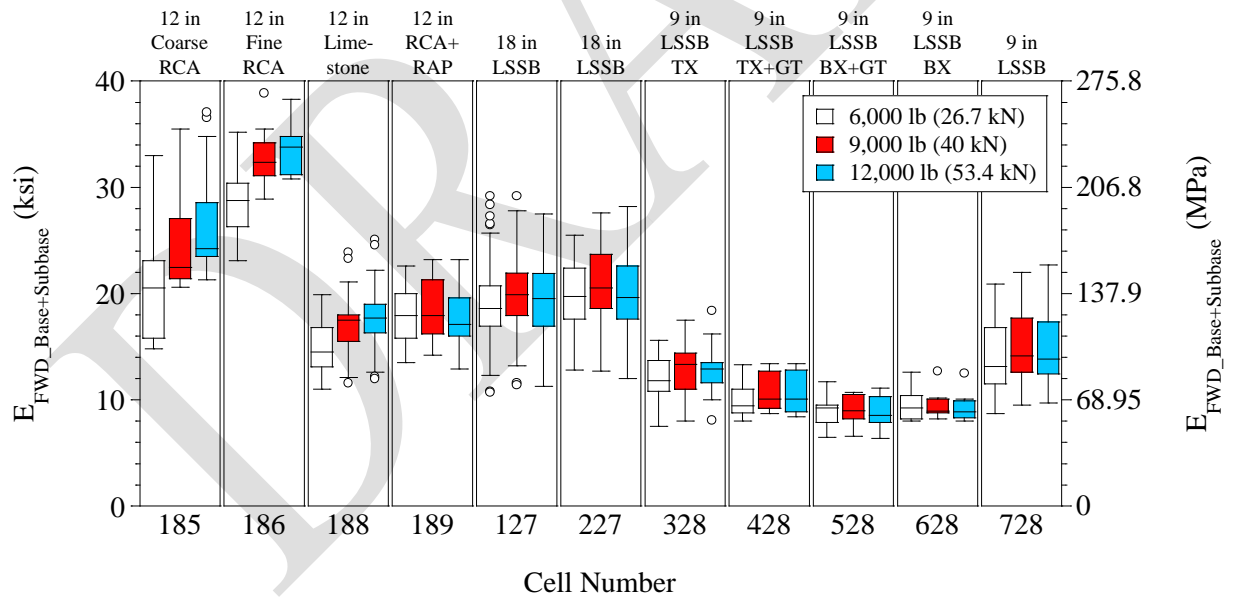


APPENDIX P. FWD TEST RESULTS OF CELLS AFTER PAVING

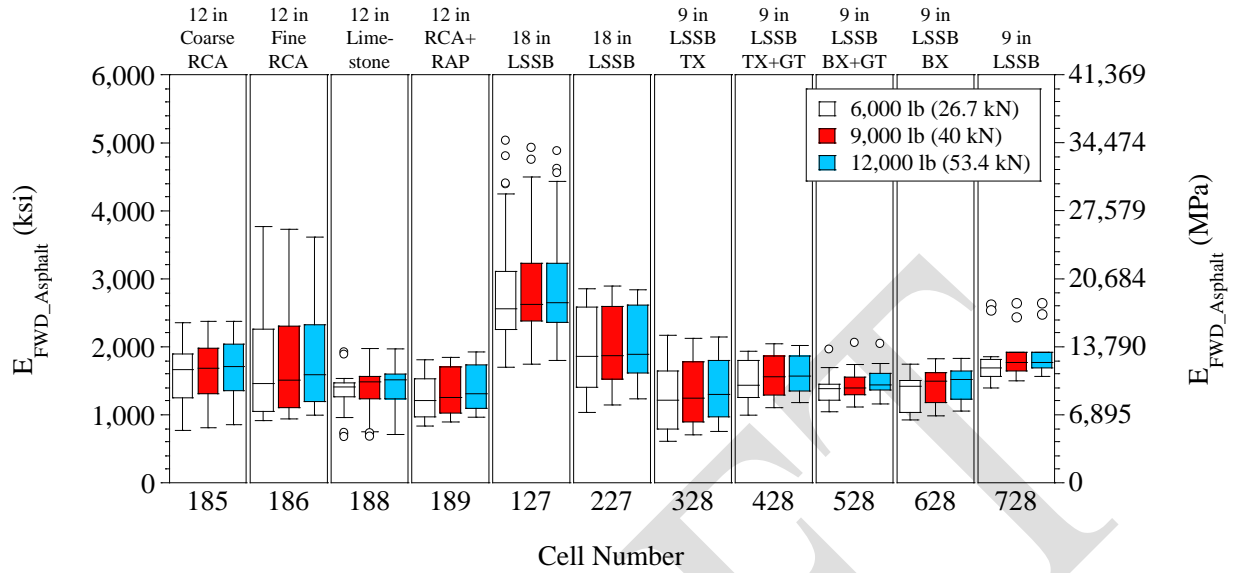
FWD Subgrade Elastic Modulus – After Paving



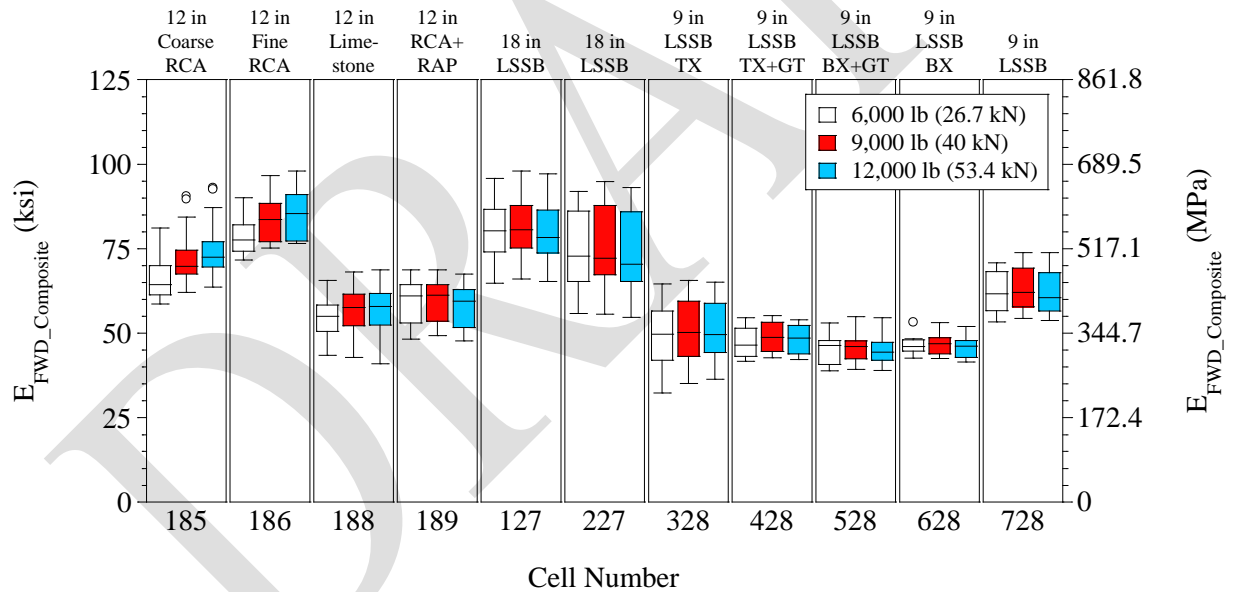
FWD Base+Subbase Elastic Modulus – After Paving



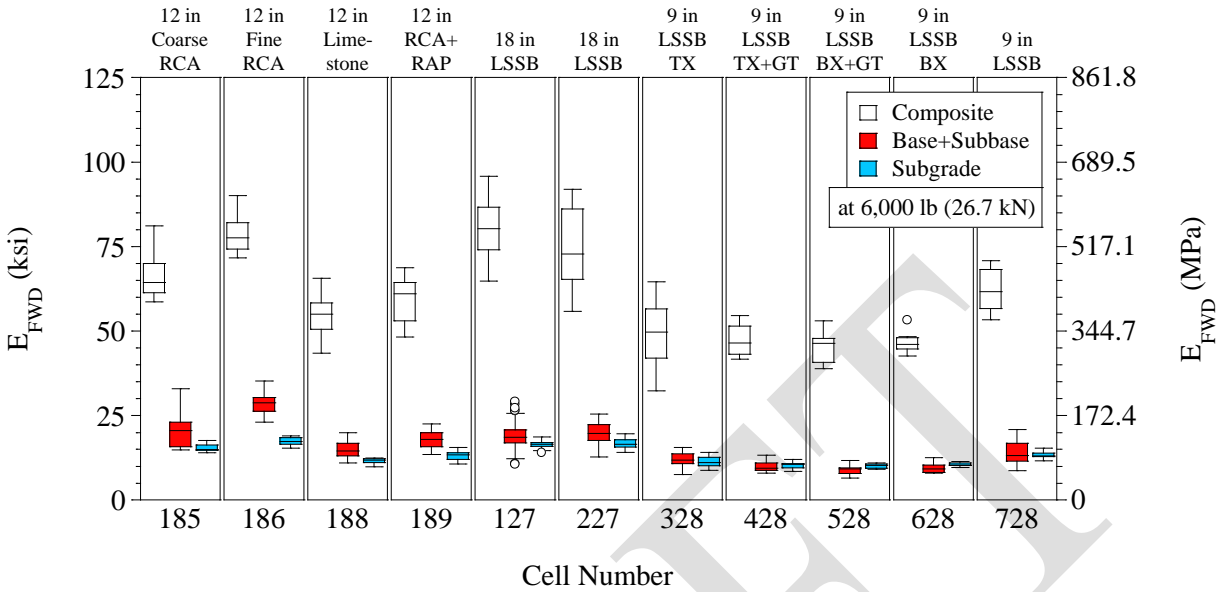
FWD Base+Subbase Elastic Modulus – After Paving



FWD Composite Elastic Modulus – After Paving



FWD Elastic Modulus at 6,000 lb (26.7 kN) – After paving



FWD Elastic Modulus at 12,000 lb (53.4 kN) – After paving

